NASA TECHNICAL NOTE

NASA TN D-7939

NASA TN D-7939

PRESSURE GRADIENT EFFECTS ON HEAT TRANSFER TO REUSABLE SURFACE INSULATION TILE-ARRAY GAPS

David A. Throckmorton

Langley Research Center
Hampton, Va. 23665

NATIONAL AERONAUTICS AND SPACE ADMINISTRATION • WASHINGTON, D. C. • AUGUST 1975

1. Report No.	2. Government Accession No.	3. Recipient's Catalog No.
NASA TN D-7939		

4. Title and Subtitle	5. Report Date
PRESSURE GRADIENT EFFECTS ON HEAT TRANSFER TO REUSABLE SURFACE INSULATION TILE-ARRAY GAPS	August 1975
	6. Performing Organization Code
7. Author(s)	8. Performing Organization Report No.
David A. Throckmorton	L-10071
	10. Work Unit No.
9. Performing Organization Name and Address	506-26-30-03
NASA Langley Research Center Hampton, Va. 23665	11. Contract or Grant No.
	13. Type of Report and Period Covered
12. Sponsoring Agency Name and Address	Technical Note
National Aeronautics and Space Administration Washington, D.C. 20546	14. Sponsoring Agency Code

15. Supplementary Notes

Part of the information presented herein was included in a thesis entitled "An Experimental Investigation of the Heat Transfer to Reusable Surface Insulation Tile-Array Gaps in a Turbulent Boundary Layer With Pressure Gradient," submitted in partial fulfillment of the requirements for the degree of Master of Science, The George Washington University, February 1975.

16. Abstract

An experimental investigation was performed to determine the effect of pressure gradient on the heat transfer within space shuttle reusable surface insulation (RSI) tile-array gaps under thick, turbulent boundary-layer conditions. Heat-transfer and pressure measurements were obtained on a curved array of full-scale simulated RSI tiles in a tunnel-wall boundary layer at a nominal free-stream Mach number of 10.3 and free-stream Reynolds numbers of 1.6, 3.3, and 6.1×10^6 per meter. Transverse pressure gradients of varying degree were induced over the model surface by rotating the curved array with respect to the flow. Definition of the tunnel-wall boundary-layer flow was obtained by measurement of boundary-layer pitot pressure profiles, wall pressure, and heat transfer.

Flat-plate heat-transfer data were correlated and a method was derived for prediction of heat transfer to a smooth curved surface (i.e., no gaps) in the highly three-dimensional tunnel-wall boundary-layer flow. Pressure on the floor of the RSI tile-array gap followed the trends of the external surface pressure. Heat transfer to the surface immediately downstream of a transverse gap is higher than that for a smooth surface at the same location. Heating to the wall of a transverse gap, and immediately downstream of it, at its intersection with a longitudinal gap is significantly greater than that for the simple transverse gap. No systematic effect of transverse pressure gradient on heating was observed. Simulation of full-scale space shuttle vehicle boundary-layer thickness and pressure-gradient level was good.

17. Key Words (Suggested by Author(s))	18. Distribution Statement
Thermal protection system (TPS) Reusable surface insulation (RSI) Space shuttle Gap heating Boundary layers	Unclassified – Unlimited Subject Category 34

19. Security Classif. (of this report)	20. Security Classif. (of this page)	21. No. of Pages	22. Price*
Unclassified	Unclassified	68	$4.25

*For sale by the National Technical Information Service, Springfield, Virginia 22161

PRESSURE GRADIENT EFFECTS ON HEAT TRANSFER TO REUSABLE SURFACE INSULATION TILE-ARRAY GAPS*

David A. Throckmorton
Langley Research Center

SUMMARY

An experimental investigation was performed to determine the effect of pressure gradient on the heat transfer within space shuttle reusable surface insulation (RSI) tile-array gaps under thick, turbulent boundary-layer conditions. Heat-transfer and pressure measurements were obtained on a curved array of full-scale simulated RSI tiles in a tunnel-wall boundary layer at a nominal free-stream Mach number of 10.3 and free-stream Reynolds numbers of 1.6, 3.3, and 6.1×10^6 per meter. Transverse pressure gradients of varying degree were induced over the model surface by rotating the curved array with respect to the flow. Definition of the tunnel-wall boundary-layer flow was obtained by measurement of boundary-layer pitot pressure profiles, wall pressure, and heat transfer.

Flat-plate heat-transfer data were correlated and a method was derived for prediction of heat transfer to a smooth curved surface (i.e., no gaps) in the highly three-dimensional tunnel-wall boundary-layer flow. Pressure on the floor of the RSI tile-array gap followed the trends of the external surface pressure. Heat transfer to the surface immediately downstream of a transverse gap is higher than that for a smooth surface at the same location. Heating to the wall of a transverse gap, and immediately downstream of it, at its intersection with a longitudinal gap is significantly greater than that for the simple transverse gap. No systematic effect of transverse pressure gradient on heating was observed. Simulation of full-scale space shuttle vehicle boundary-layer thickness and pressure-gradient level was good.

INTRODUCTION

The space shuttle orbiter is being designed for an operational life in excess of 100 reentry missions with minimal refurbishment between those missions. In order to

*Part of the information presented herein was included in a thesis entitled "An Experimental Investigation of the Heat Transfer to Reusable Surface Insulation Tile-Array Gaps in a Turbulent Boundary Layer With Pressure Gradient," submitted in partial fulfillment of the requirements for the degree of Master of Science, The George Washington University, February 1975.

meet this requirement, the vehicle thermal protection system (TPS) will be a surface covering of a nonmetallic, low-density refractory oxide. This material, referred to as reusable surface insulation (RSI), must be capable of withstanding, without degradation, repeated exposure to the harsh reentry environment, while insulating the structure of the vehicle from surface temperatures in excess of 1500 K. The material will be attached to the vehicle surface in a "brick-like" array of square tiles (15.25 by 15.25 cm) which vary in thickness from approximately 1 to 10 centimeters according to the intensity of the local heating. Small gaps between tiles will allow for thermal expansion of the tile material. Interference heat transfer to the tile exterior and gap wall surfaces is of major concern to the TPS designer. The presence of the gaps may result in increased boundary-layer turbulence and attendant increased surface heating. Heating levels within the gaps, which would be expected to be substantially lower than surface values, may approach surface values due to flow reattachment phenomena. In addition, radiation blockage within the gaps may produce extreme temperatures even at low heating levels, and the shortened heat paths (i.e., from gap wall instead of tile exterior surface) may result in excessive bond-line temperatures.

Effective design of the TPS requires a sound knowledge of the aerodynamic heating environment to which the RSI tiles will be subjected. This knowledge must include an accurate definition of the heat-transfer distribution within the tile gaps and a good understanding of how this distribution is affected by boundary-layer state (laminar/turbulent), boundary-layer thickness, flow angularity, gap width, tile edge radius, tile stacking arrangement, and other parameters.

As a part of the space shuttle development program, an experimental effort has been focused on the shuttle-related gap heating problems. Evaluation of TPS tile material thermal performance (ref. 1) and definition of the gap heating environment are important elements in this effort. Johnson (ref. 2) studied the effects of gap width and boundary-layer thickness on TPS gap heating for turbulent flow over a simulated tile array at Mach 8. This work revealed a potential heating problem area at the intersection of streamwise and transverse gaps. The present author obtained data on a simulated tile array in a turbulent boundary layer to investigate the effects of gap width, flow angularity, and tile surface mismatch on tile gap heating. (See ref. 3.) Foster et al. (ref. 4) investigated the effect of similar parameters for single gaps and gap intersections in laminar flow. A compilation and analysis of these and other recent gap heating data may be found in reference 5.

Because of entry angles of attack and the complex curvatures of the orbiter external surface, boundary-layer flows over much of the flight vehicle will be strongly influenced by surface pressure gradients. Each of the recent studies of TPS gap heating phenomena, however, has been conducted on sharp-leading-edge flat plates or in tunnel-wall boundary

layers under conditions of zero pressure gradient. The present investigation was undertaken to assess possible effects of pressure gradient on the heat transfer to RSI tile-array gaps in a thick, turbulent boundary layer.

Heat-transfer and pressure-measurement tests were made on a curved array of full-scale simulated RSI tiles submerged in a thick, turbulent, tunnel-sidewall boundary layer. Transverse pressure gradients of varying degree were induced over the model surface by rotating the curved array with respect to the flow direction. This enabled the study of RSI tile-array gap heating as affected by pressure gradient. The tile-array model was tested both with gaps present, and with the gaps filled and smoothed to provide smooth-surface reference data. Heat-transfer and pressure measurements were also made on a flat plate mounted in the tunnel sidewall. These data, along with measured pitot pressure profiles, provided a definition of the characteristics of the three-dimensional boundary-layer flow in which the tile-array tests were conducted.

SYMBOLS

A	constant in equation (7), cm^{-1}
B	constant in equation (7)
c_p	constant pressure specific heat of air, J/kg-K
$c_{p,m}$	specific heat of model material, J/kg-K
d	depth into gap, cm (see fig. 5)
h	heat-transfer coefficient, W/m^2-K
k	constant in equation (14)
L	full-scale tile dimension, cm
M	Mach number
N_{St}	Stanton number, $h/\rho_w u_e c_p$
P	pressure, N/m^2
$P_{t,2}$	total pressure behind a normal shock in the free stream, N/m^2

q	heat-transfer rate, W/m^2
$\overline{R}$	universal gas constant, $m^2/sec^2\text{-}K$
$R_{w,\theta}$	Reynolds number based on wall conditions and boundary-layer momentum thickness, $\rho_w u_e \theta/\mu_e$
R_∞	free-stream Reynolds number, $\rho_\infty u_\infty/\mu_\infty$, m^{-1}
r	recovery factor
S	surface dimension defined in figure 30, m
T	temperature, K
t	time, sec
u	velocity, m/sec
X,Y,Z	coordinate system defined in figure 10
x,y,z	coordinate system defined in figures 3 and 10
Y_{max}	maximum vehicle planform dimension defined in figure 30, m
z_{surf}	z-dimension of local curved model surface, cm
α	array rotation angle, deg (see fig. 10)
γ	ratio of specific heats of air
δ^*	boundary-layer displacement thickness, cm
δ^*_{eff}	"effective" boundary-layer displacement thickness defined in equation (14), cm
θ	boundary-layer momentum thickness, cm
λ_m	model material thickness, m

μ viscosity, N-sec/m^2

ρ density of air, kg/m^3

ρ_m model material density, kg/m^3

ϕ angle between surface tangent plane and flow velocity vector, deg

Subscripts:

aw adiabatic wall

e boundary-layer edge

fp flat plate

sm surface of the smooth, curved array

t total

w wall

∞ free stream

APPARATUS AND TESTS

Facility

The experimental results presented herein were obtained in the Langley continuous flow hypersonic tunnel. This facility, which has a 78.74-cm square test section, operates at a nominal free-stream Mach number of 10.3 over a free-stream Reynolds number range of 1.5 to 8.2×10^6 per meter using air as the test gas, and may be operated in either a blowdown or continuous, closed-circuit mode. To prevent liquefaction, the air is heated by use of electrical resistance tube bundles. The tunnel-throat, expansion, and diffuser sections are all water cooled. A photograph of the facility test section is presented in figure 1.

For these tests, the models were mounted on the model injection mechanism which is shown adjacent to the test section in figure 2. This device allows a model to be isolated from the hypersonic airstream for model cooling or configuration changes while

the tunnel is operating. The mechanism also provides rapid injection of a model into the hypersonic airstream.

Models

Pressure-gradient model.- The RSI tile pressure-gradient model was a curved array of simulated full-scale RSI tiles fabricated of Inconel sheet with a nominal thickness of 0.0483 cm. Surface curvature was generated from a right circular cylinder of 102.28-cm radius, cut by a plane at a 5° angle to the axis of the cylinder. A schematic drawing of the model is shown in figure 3. Individual tile size was 14.92 cm square.

The model was fabricated such that each transverse row of simulated tiles was a continuous sheet of material with the longitudinal gaps formed by bending. The transverse gaps were fabricated separately and electron-beam welded between tile row sections to form the complete tile array. Stress relief in the material following the welding process resulted in a "pinching down" of the transverse gaps from the desired width. Resulting gap width between tiles was nominally 0.30 cm for longitudinal gaps and 0.20 cm for transverse gaps. Gap depth was 2.86 cm.

Spacer plates were also fabricated to maintain model edges flush with the tunnel sidewall. Three sets of spacer plates were fabricated to allow testing at model flow angularities of 0°, $\pm 22.5^{\circ}$, and $\pm 45^{\circ}$. The model and spacer plates mounted on the facility injection system are shown in figure 4.

The model was instrumented with 67 chromel-alumel thermocouples spotwelded to the model back surface at tile-surface and gap locations indicated in figure 5. The model was also fitted with 12 static pressure orifices (7 located on the surface of a tile and 5 located on the floor of a transverse gap) as indicated in figure 5. Precise thermocouple and pressure orifice locations are listed in table I.

For smooth-surface testing of the model, the gaps were eliminated by filling them with twine to a point approximately one gap width below the tile exterior surface. The remainder of the gap was filled with plaster of paris which was allowed to dry and then smoothed by sanding to match the surrounding surface. This created a smooth model with correct curvature for measurement of surface reference data.

Flat-plate model.- A smooth flat-plate model, used to measure undisturbed wall-heat-transfer coefficients, was fabricated from 321 stainless steel sheet with a nominal thickness of 0.127 cm. The 50.8-cm square panel fit flush with the injection plate fabricated for testing of this model. The model and injection plate are shown mounted on the injection strut, ready for testing, in figure 6. The flat-plate model was instrumented with 11 chromel-alumel thermocouples spotwelded to the model back surface, located as shown in figure 7.

Boundary-layer probe.- An 11-tube pitot-probe rake was placed downstream of the flat-plate model at four spanwise locations. Individual pitot probes were located at stations normal to the wall as shown in figure 8. Tube diameters varied with position relative to the wall. The rake is shown installed with the flat-plate model for testing in figure 6.

Instrumentation

Temperature data were obtained using the chromel-alumel thermocouples with a reference junction of 324.8 K. The reference-junction temperature was thermostatically controlled to within ±0.55 K.

Pressures were measured using baratrons mounted on the injection strut immediately behind the model. The baratron is a capacitance-type transducer, operated in conjunction with a signal conditioner to allow measurement of pressure over seven ranges from 0 to 68.9 N/m^2 to 0 to 68.9 kN/m^2. The signal conditioner provides automatic ranging such that the measurements were obtained on the lowest possible range. Measurement accuracy is estimated to be within ±7 percent of reading.

Test Procedures and Conditions

The transient-calorimeter technique was used to measure heat-transfer rates to the surfaces of the thin-skin models. The tests were conducted with the models initially at room temperature, isolated from the hypersonic airstream within the injection chamber, at a pressure equal to the test-section static pressure. With the hypersonic flow established in the test section, the model was rapidly injected to the test position, flush with the tunnel sidewall, and temperature and pressure data were automatically recorded on magnetic tape by an analog-to-digital converter at a rate of 20 samples per second. The model was exposed to the airstream for an interval of time sufficient to allow pressure transducer outputs to "settle out," and then retracted.

Both the tile-array and flat-plate reference models were tested at total pressures within the settling chamber of 2.41, 5.17, and 9.65 MN/m^2, corresponding to free-stream Reynolds numbers of 1.6, 3.3, and 6.1×10^6 per meter. Additional flat-plate data were obtained at a total pressure of 12.07 MN/m^2 (Reynolds number of 7.4×10^6 per meter). The tile-array model was tested at flow angles α of 0^o, $\pm 22.5^o$, and $\pm 45^o$. Testing at positive and negative flow angles allowed measurement of both temperature and pressure data over the entire model surface while instrumenting only one side of the plane of symmetry for either temperature or pressure as shown in figure 5. By "mirror imaging" the data obtained at negative flow angles, data for the entire model surface were obtained for flow angles of $\alpha = 0^o$, 22.5^o, and 45^o.

DATA REDUCTION

Boundary-Layer Profiles

Boundary-layer velocity and density profiles were derived from wall boundary-layer pitot pressure measurements. These calculations required assumptions of the distribution of static pressure and temperature through the boundary layer. As shown in figure 9, the measured wall static pressure was significantly higher than the free-stream static pressure computed from one-dimensional flow considerations. However, pressure measurements in the free stream of the facility (ref. 6) show good agreement with the computed free-stream static pressure. Static pressure within the boundary layer was assumed to vary linearly between the measured wall and computed free-stream values.

Total temperature within the boundary layer was assumed to vary as the square of velocity, that is,

$$\frac{T_t - T_w}{T_{t,e} - T_w} = \left(\frac{u}{u_e}\right)^2 \tag{1}$$

which is characteristic of turbulent tunnel-wall boundary layers (ref. 7). Unpublished total temperature measurements made by D. H. Crawford in the wall boundary layer of this facility show good agreement with the quadratic temperature-velocity relation.

With the measured pitot pressure and assumed static pressure at each point, the Rayleigh pitot equation was applied to calculate local Mach number. Local velocity and density were then computed using the assumed temperature distribution and the perfect-gas equation of state.

Heat-Transfer Data

The test procedure of rapid injection of the isothermal model to the test position provided a step input in heat transfer to the thin-skin model. Heat-transfer rates were determined by the transient-calorimeter technique of measuring the time rate of change of the model skin temperature. For data reduction purposes, the one-half second interval of temperature data immediately following model injection was disregarded to allow flow conditions to stabilize in the gap. This time is in excess of the required time as reported by Nicoll (ref. 8). A quadratic least-squares curve was fit to the subsequent 4-sec interval of data for each thermocouple. Rates of change of temperature with time $\partial T_w/\partial t$ were evaluated analytically from the curve-fit expressions at the initial point of each curve fit. Heat-transfer rates were then computed from the expression

$$q = \rho_m c_{p,m} \lambda_m \frac{\partial T_w}{\partial t} \tag{2}$$

The long interval (4 sec) of temperature-time data used for heat-transfer rate calculation allowed measurement of the low heating rates found within the gaps which were not discernible when a shorter interval (1 sec) of data was considered. An assessment of conduction effects which result from the long data interval, for representative data from this test, indicates a maximum error in computed heating rate of less than 10 percent for the "worst case" thermocouple.

Heat-transfer data are expressed in the form of the heat-transfer coefficient h defined as

$$h = \frac{q}{T_{aw} - T_w} \tag{3}$$

Adiabatic wall temperature T_{aw} was computed from the relation

$$r = \frac{T_{aw} - T_\infty}{T_t - T_\infty} \tag{4}$$

where recovery factor r was assumed equal to 0.89 for the turbulent test conditions. This relation was applied to both flat-plate and curved-array data.

RESULTS AND DISCUSSION

Coordinate Definition

In the discussion of experimental results which follows, the data are referenced to coordinate systems defined in figure 10. All flat-plate and wall boundary-layer data are referenced to a stream-oriented coordinate system (X,Y,Z) which is fixed within the flow. All curved-panel data, both smooth and with gaps present, are referenced to a coordinate system (x,y,z) fixed within the rotating curved array. The origins of both coordinate systems are located on the tunnel sidewall at the center of rotation of the tile-array model. The coordinate pairs of any point (x,y and X,Y) are related by the rotation transformation:

$$X = x \cos \alpha - y \sin \alpha$$

$$Y = x \sin \alpha + y \cos \alpha$$

Boundary-Layer Surveys

Boundary-layer velocity profiles measured on the sidewall center line are presented in figure 11 for the four free-stream unit Reynolds numbers at which flat-plate data were obtained. The profile shapes are characteristic of a fully developed turbulent boundary layer and the profiles tend to "fill out" (boundary-layer thins) with increasing unit Reynolds number. Profiles obtained at several transverse locations at a single unit Reynolds number are compared in figure 12. A significant change in the boundary-layer profile shape as a function of transverse position is observed. This transverse variation in boundary-layer profile is an indication of the three-dimensional character of the boundary-layer flow in a nozzle of square cross section. The three dimensionality results from the corner interaction of the tunnel sidewall, floor, and ceiling boundary layers.

The measured profile data were integrated to obtain values of the bulk quantities of boundary-layer displacement δ^* and momentum θ thicknesses, defined by the relations

$$\delta^* = \int_0^\infty \left(1 - \frac{\rho u}{\rho_e u_e}\right) dZ \tag{5}$$

$$\theta = \int_0^\infty \left(1 - \frac{u}{u_e}\right) \frac{\rho u}{\rho_e u_e} \, dZ \tag{6}$$

The variations of these quantities with free-stream unit Reynolds number and transverse position are presented in figure 13. Momentum thickness decreases, as expected, with increasing unit Reynolds number, and shows little transverse variation. Boundary-layer displacement thickness does not change significantly with unit Reynolds number, but does, however, decrease rapidly with transverse position reflecting the changes in boundary-layer profile shape noted in figure 12.

Flat-Plate Results

Heat-transfer data.- Measured flat-plate heat-transfer coefficients are shown in figure 14 for the full range of test conditions. At each Reynolds number, the heat transfer increases in the transverse direction, primarily as a result of the thinning of the boundary layer, and is symmetric about the center line. The streamwise distribution of heat transfer shows a small heating decrease characteristic of a fully developed, thickening boundary layer.

Pressure data.- The flat-plate pressure data (fig. 15) show a transverse distribution similar to that of the heat-transfer data. Streamwise, however, the pressure decreases to a minimum and increases in the downstream (+X) direction. This behavior is attributed to the fact that the test-section area of this facility does not represent a complete expansion of the flow from the tunnel throat. The tunnel nozzle expands the flow to a point approximately 1 meter upstream of the test-section center, at which the flat, parallel walls of the test section begin. The intersection of the expansion-section and test-section walls then constitutes a compression corner for the wall boundary-layer flow. The data presented herein were obtained in the compression region downstream of this corner.

Flat-plate data correlation.- In order to understand the mechanisms controlling the wall boundary-layer heat transfer, the heating data of figure 14 were correlated with parameters which could be expected to influence heat transfer. Figure 16 presents flat-plate heating data expressed in the form of Stanton number N_{St} plotted as a function of Reynolds number based on wall conditions and boundary-layer momentum thickness $R_{w,\theta}$. The heat-transfer data points were inferred from the data of figure 14 for the transverse locations at which boundary-layer profiles were obtained.

At each transverse location, Stanton number and Reynolds number correlate the data over the range of free-stream flow conditions with Stanton number varying as the wall Reynolds number $R_{w,\theta}$ to the -0.07 power as indicated in figure 16. Failure to correlate the data for the three transverse locations is not surprising, as the Stanton-Reynolds number correlation relates changes in streamwise variables and has no application to transverse flow phenomena. The upstream histories of the boundary layers affecting each transverse location are unique and no simple boundary-layer parameter relates the transverse influence of boundary-layer characteristics. The single parameter which varies significantly in the transverse plane is boundary-layer displacement thickness, and, for a given boundary-layer flow, heat transfer is known to decrease with increasing boundary-layer thickness. As previously noted, for this tunnel-wall flow, displacement thickness does not vary significantly with unit Reynolds number. The effect of transverse-boundary-layer-thickness variation on tunnel-sidewall heat transfer is indicated in figure 17 where the data of figure 16 are presented as a function of displacement thickness. The flat-plate heat-transfer data correlate with pertinent flow variables according to the relation

$$N_{St}R_{w,\theta}^{0.07} = A\delta^* + B \tag{7}$$

where

$$A = -0.000277 \text{ cm}^{-1}$$

$$B = 0.00466$$

This expression quantifies the relationship between measured boundary-layer parameters and measured wall heat transfer for this tunnel-wall flow. The correlation has no application to any flow other than this tunnel-wall boundary layer; however, it indicates a good understanding of this flow and lends confidence to the curved-array data which follow.

RSI Tile Array – Smooth-Model Data

Because of the complexity of the wall boundary-layer flow indicated by the flat-plate and boundary-layer-probe results, heat-transfer and pressure data were obtained on the RSI tile-array model with no gaps present. These data were used to relate measured surface and gap heating to an undisturbed surface reference.

Pressure data.- Smooth-model pressure data and fourth-order least-squares curve fits of the data are presented in figure 18 for all test conditions. The data from the orifice located at $y = \pm 5.08$ cm were not considered for computation of the curve-fit expressions as data from this transducer were consistently higher than those from the other transducers. At an array rotation angle α of 0°, the pressures show the same transverse trends demonstrated by the flat-plate data. Flow deflection angle ϕ (i.e., the angle between the free-stream velocity vector and the plane of tangency of the surface at a point) has negligible point-to-point variation between orifices when $\alpha = 0^{\circ}$. With increases in rotation angle to 22.5° and 45°, flow deflection angles on the upstream portion of the model increase, those on the downstream portion decrease, and static pressures vary accordingly.[1]

Heat-transfer data.- Measured smooth-surface reference heat-transfer data are presented in figure 19 for the curved-array model. For the zero-rotation case, the flat-plate heating data are also presented for comparison. Because of the 5° surface inclination of the curved panel, heat transfer to the panel was greater (as shown) than to the flat plate. Based on the flat-plate results, the increase in heat transfer with transverse distance from the center line was expected. However, at $\alpha = 0^{\circ}$ the rate of increase in the transverse direction was expected to be nearly equal to that for the flat plate since flow deflection angle remains constant with transverse position. As figure 19 ($\alpha = 0^{\circ}$) shows, the transverse rate of increase of heating to the curved array is significantly greater than that for the flat plate. This more rapid increase is hypothesized to be the result of an effective "thinning" of the boundary layer due to the protrusion of the model into the boundary-layer flow. With a boundary layer which is much thicker than the protruding height of the tile-array model, it is not thought that the model will significantly affect

[1]Note that the y-coordinate is fixed in the rotating array, while the Y-coordinate is fixed in the tunnel sidewall. While y-values are constant for each orifice, the orifice locations within the complex boundary-layer flow vary with array rotation angle. Therefore, the pressure and heat-transfer variations shown in the figures as functions of the y-coordinate are a superposition of effects of changing flow deflection angle and changes in the Y-coordinate position (boundary-layer conditions affecting the point).

the outer portions of the boundary layer as would be the case if the characteristic dimension of the model was of the same order as the boundary-layer thickness. Rather, the boundary-layer edge location remains essentially unchanged from the flat-plate case and the boundary-layer thickness is decreased by the protrusion of the curved model into the flow.

Smooth-surface heating data for the $\alpha = 22.5^{\circ}$ and 45° cases show increased surface heating with increasing flow deflection angle (y increasing) as expected. The data also show, however, increases in heating where the flow deflection angle is decreasing (y decreasing). This anomaly is explained by the fact that these heating increases, in regions of decreasing flow deflection, are occurring at wall positions where boundary-layer thickness is decreasing. The opposing effects of decreasing boundary-layer thickness and flow deflection angle are dominated by the boundary-layer thinning effect, and heating increases. In the following section, a method will be developed to predict smooth-model-surface heat transfer.

Prediction of smooth-surface heating characteristics.- Consider the correlation of flat-plate heating data presented in figure 17

$$N_{St}R_{w,\theta}^{0.07} = A\delta^* + B$$

and assume that a correlation of this form is valid for the smooth-curved-panel data. Therefore, for curved-panel data,

$$\frac{N_{St}R_{w,\theta}^{0.07}}{\left(N_{St}R_{w,\theta}^{0.07}\right)_{fp}} = \frac{A\delta_{eff}^* + B}{(A\delta^* + B)_{fp}} \tag{8}$$

where δ_{eff}^* is an effective boundary-layer thickness as hypothesized in the previous section. By definition,

$$\left.\begin{aligned} N_{St} &\equiv \frac{h}{\rho_w u_\infty c_p} \\ R_{w,\theta} &\equiv \frac{\rho_w u_\infty \theta}{\mu_w} \end{aligned}\right\} \tag{9}$$

Substituting these expressions in equation (8) and assuming $u_\infty \approx u_{\infty,fp}$,

$$\left[\frac{h/\rho_w}{(h/\rho_w)_{fp}}\right]\left[\frac{\rho_w\theta/\mu_w}{(\rho_w\theta/\mu_w)_{fp}}\right]^{0.07} = \frac{A\delta^*_{eff} + B}{(A\delta^* + B)_{fp}} \tag{10}$$

Assuming a perfect gas,

$$\rho = \frac{P}{RT} \tag{11}$$

and assuming wall-temperature variations are negligible,

$$T_w \approx T_{w,fp}$$

and

$$\mu_w \approx \mu_{w,fp}$$

Then,

$$\left[\frac{h/P}{(h/P)_{fp}}\right]\left[\frac{P\theta}{(P\theta)_{fp}}\right]^{0.07} = \frac{A\delta^*_{eff} + B}{(A\delta^* + B)_{fp}} \tag{12}$$

Neglecting the weak dependence on θ

$$\frac{h}{h_{fp}} = \left(\frac{P}{P_{fp}}\right)^{0.93} \frac{A\delta^*_{eff} + B}{(A\delta^* + B)_{fp}} \tag{13}$$

Now, estimate

$$\delta^*_{eff} = \delta^* - kz_{surf} \tag{14}$$

where z_{surf} is the local protrusion of the smooth model surface into the boundary-layer flow, and k is an unknown constant.

If the value of the constant k and the local pressure on the curved array are known, the distribution of heat transfer to the surface of the smooth curved panel may be predicted using equations (13) and (14) with the measured flat-plate pressure, heat transfer, and boundary-layer data. Surface pressure was measured, however, on one transverse ray of the smooth curved panel. Figure 20 presents measured heat-transfer data for that ray

for a Reynolds number of 3.3×10^6 per meter, along with the predicted heating from equations (13) and (14), using the measured pressure data. The value of the constant k which provided a "best fit" to the experimental data was 0.5. The predicted heat transfer shows excellent agreement with the experimental data. Similar results were observed in the data obtained at Reynolds numbers of 1.6 and 6.1×10^6 per meter.

RSI Tile-Array Results – Gaps Present

Pressure data.- Measured pressures for the simulated RSI tile array are presented in figure 21 for all test conditions. Tile-surface data are shown as open symbols and gap-floor data, as solid symbols. Comparison of these data with those of figure 18 indicates that the surface pressure distributions with gaps present are essentially identical to those obtained with a smooth model. Pressure level within the gaps closely follows that of the tile exterior surface.

Gap heat-transfer data.- Measured distributions of heat transfer[2] along the instrumented transverse gap are shown in figures 22 to 24 for each array rotation angle and Reynolds number. For the zero-rotation case (fig. 22), at transverse positions off the center line ($y \neq 0$), no intense reattachment heating occurs at the gap corner, and no significant increase in surface heating occurs downstream of the transverse gap, indicating negligible flow separation over the transverse gap. Note also that off the center line at a depth into the gap of less than four gap widths (△-symbol), the local heating level is less than 2 percent of the undisturbed surface value. The solid symbols in figures 22 through 29 indicate extremely low heat-transfer-rate data which are of questionable accuracy. These data are included for completeness.

For the zero-rotation case (fig. 22) on the array center line ($y = 0$) the gap geometry consists of a longitudinal gap intersecting the transverse gap. Heat transfer to the transfer gap at the intersection point and to the tile surface immediately downstream of the gap is significantly higher than for a simple transverse gap as exists away from the center line. This heating increase at the gap intersection is attributed to a large region of flow separation within the longitudinal gap and a strong shear-layer reattachment on the forward-facing wall of the transverse gap. Heating at the intersection point is dependent upon Reynolds number. Dunavant and Throckmorton (ref. 9), using gap-intersection data from several facilities, have shown that such data may be correlated as a function of boundary-layer displacement thickness, streamwise-gap running length, gap width, and depth location within the gap.

---

[2]All heat-transfer data discussed in this section are nondimensionalized by the measured heat transfer to the smooth-surface model. Surface data are normalized by the smooth-model measurement of the same thermocouple; gap-wall data are normalized by the smooth-model-surface measurement at the thermocouple location nearest the gap.

Rotation of the tile array (figs. 23 and 24) produces increased surface reattachment heating immediately downstream of the transverse gap. As in the zero-rotation case, the surface reattachment heating is most severe downstream of the longitudinal-gap—transverse-gap intersection. Within the gap, array rotation does not significantly affect the level of heat transfer, but it does result in a transverse shift of the heating peak on the gap wall downstream of the longitudinal gap, toward the low-pressure side of the gap intersection. Again, the heating level in this region of flow reattachment is dependent upon Reynolds number.

Figures 25 and 26 present heat-transfer data for the longitudinal gap at each Reynolds number as a function of array rotation angle. The significant variations in gap heating observed in these plots result from the change in orientation of the wall, from one which is forward facing to one which is rearward facing, as array rotation angle changes. With the exception of certain low Reynolds number data, when the wall is rearward facing ($\alpha > 0^{o}$), the flow appears to separate upstream of the tile gap corner, resulting in substantially lower heating to the corner (Δ-symbol) than to the undisturbed surface. When the wall is forward facing ($\alpha < 0^{o}$), the flow reattaches in the vicinity of the corner resulting in heating equal to or greater than the undisturbed surface value.

At $\alpha = -45^{o}$ the longitudinal gap (figs. 25 and 26) presents nearly the same geometry to the flow as does the transverse gap at $\alpha = 45^{o}$ (fig. 24, y = 3.81 cm). However, the gap-corner flow reattachment observed for the longitudinal gap was not present on the transverse gap. These contrasting results are attributed to differences in the gap width and corner radii between the longitudinal and transverse gaps. As a result of the model fabrication process discussed previously, longitudinal gap width was approximately 1.5 times as large as transverse gap width and longitudinal gap edge radius was larger than that of the transverse gap. The increased gap width and large exposed surface area at the longitudinal gap edge allow for diffusion of a shear layer into the gap and flow reattachment at the tile corner as opposed to the negligible separation and reattachment observed for the transverse gap.

The variations of gap heat transfer with rotation angle for the simple transverse gap and the gap intersection are presented in figures 27 and 28, respectively. Array rotation angle has little effect upon the heating within the simple transverse gap (fig. 27), but tends to increase slightly the heating to the surface immediately downstream of the gap. For the gap intersection location (fig. 28) at the lower Reynolds numbers, array rotation again has minimal effect on heating within the gap. However, at the highest Reynolds number (fig. 28(c)) array rotation decreases the gap heating level at the gap intersection. It should be noted that this heating decrease is a result of the previously discussed shift of the heating peak within the gap (figs. 22 to 24), and does not reflect a lessening of the heating load within the gap. Figure 28 also clearly demonstrates the large increase in

tile surface heating which occurs immediately downstream of a longitudinal-gap—transverse-gap intersection. All surface data of figure 28 are significantly higher than the corresponding data for the simple transverse gap (fig. 27).

Pressure-Gradient Effects on Gap Heat Transfer

Rotation of the curved array not only produced crossflow over the array, but also the desired pressure gradient within the gap. The magnitude of this pressure gradient was determined by differentiating the curve fits of the gap pressure data of figure 21. In figure 29 measured heat transfer in the transverse gap at $y = \pm 3.81$ and ± 11.43 cm is presented as a function of a nondimensional pressure-gradient parameter. This parameter $\frac{\partial P}{\partial y}\frac{L}{P}$ is the local pressure gradient divided by the local pressure times some characteristic length. Using the full-scale tile dimension as the characteristic length ($L = 15.24$ cm), this parameter is physically the nondimensionalized pressure drop for one tile length along the gap. No systematic effect of pressure gradient on gap heat transfer is evident.

Shuttle Pressure-Gradient and Boundary-Layer Simulation

In order to evaluate the full-scale shuttle pressure-gradient simulation obtained with the curved-array model, full-scale-vehicle spanwise pressure distributions were obtained at two longitudinal stations. These pressure distributions were calculated, using the method of reference 10, for a full-scale vehicle at Mach 10.0 and 30° angle of attack in an ideal gas with $\gamma = 1.12$. The surface pressure distributions were numerically differentiated to obtain the full-scale values of the pressure-gradient parameter $\frac{\partial P}{\partial S}\frac{L}{P}$. Values of this parameter for the full-scale vehicle are presented in figure 30 as a function of surface dimension S/Y_{max} for the two longitudinal stations illustrated. The shaded area superimposed upon these data indicates the range of pressure-gradient parameter values obtained in the wind-tunnel tests. Simulation of full-scale-vehicle pressure-gradient levels is excellent with the exception of the wing leading-edge regions. Wing leading-edge TPS, however, will be a solid material with no gaps present, therefore, pressure gradient is not of concern on that portion of the vehicle surface.

Reference 5 indicates that although the boundary-layer edge Mach number and unit Reynolds numbers of the present tests are more extreme than expected in flight, the boundary-layer displacement and momentum thicknesses provide good simulation for a range of flight body-point—trajectory-point combinations.

CONCLUDING REMARKS

An experimental investigation has been conducted to assess the effect of pressure gradient on the heat transfer to reusable surface insulation (RSI) tile-array gaps submerged in a thick, turbulent boundary layer. The experimental program consisted of heat-transfer and pressure measurements on a curved array of full-scale simulated RSI tiles in the tunnel-wall boundary layer of the Langley Research Center continuous flow hypersonic tunnel over a range of free-stream Reynolds numbers and flow angularities. The tile-array model was tested with gaps present, and with gaps eliminated to obtain smooth-surface reference data under conditions simulating full-scale-vehicle pressure gradients. In order to gain a thorough understanding of the boundary-layer flow in which these tests were conducted, pitot profile measurements of the tunnel-wall boundary layer and wall-pressure and heat-transfer measurements were made.

Because of corner effects in the square cross section contoured nozzle, the wall boundary layer of the continuous flow hypersonic tunnel is highly three dimensional with significant transverse thickness variations. However, the measured flat-plate wall heat transfer correlated with momentum-thickness Reynolds number and boundary-layer displacement thickness. Heating to the curved tile array in this flow was more sensitive to transverse position than was the flat-plate heating. This sensitivity resulted from thinning of the boundary layer by the protrusion of the curved surface into the flow. A method was developed for prediction of smooth-curved-array heat transfer in this tunnel-wall boundary-layer flow. The method uses an estimated or measured surface pressure to perturb the measured flat-plate heating data, and accounts for "effective" boundary-layer thinning due to the protrusion of a model into the boundary layer. Simulations of full-scale space shuttle transverse pressure gradient and boundary-layer thickness were good.

The results of this investigation indicate the following:

1. The level and distribution of pressure on the floor of the RSI tile-array gaps follow the trends of pressure on the external tile surface.

2. Heat transfer to a forward-facing transverse-gap wall is significantly higher at the intersection of a longitudinal and transverse gap than for a simple longitudinal or transverse gap.

3. Heat transfer to the tile surface immediately downstream of a transverse gap is higher than for the smooth surface with no gaps present. The increased surface heating due to the gaps is particularly significant downstream of a longitudinal-gap—transverse-gap intersection.

4. For a thick, turbulent boundary layer there is no systematic effect of transverse pressure gradient on tile-array-gap heat transfer.

Langley Research Center,
National Aeronautics and Space Administration,
Hampton, Va., April 14, 1975.

REFERENCES

1. Brewer, R. A.; Saydah, A. R.; Nestler, D. E.; and Florence, D. E.: Thermal Performance Evaluation of RSI Panel Gaps for Space Shuttle Orbiter. J. Spacecraft & Rockets, vol. 10, no. 1, Jan. 1973, pp. 23-28.

2. Johnson, Charles B.: Heat Transfer Data to Cavities Between Simulated RSI Tiles at Mach 8. NASA CR-128770, 1973.

3. Throckmorton, David A.: Heat Transfer to Surface and Gaps of RSI Tile Arrays in Turbulent Flow at Mach 10.3. NASA TM X-71945, 1974.

4. Foster, Thomas F.; Lockman, William K.; and Grifall, William J.: Thermal Protection System Gap Heating Rates of the Rockwell International Flat Plate Heat Transfer Model (OH2A/OH2B). NASA CR-134077, 1973.

5. Christensen, H. E.; and Kipp, H. W.: Data Correlation and Analysis of Arc Tunnel and Wind Tunnel Tests of RSI Joints and Gaps. Volume 1 – Technical Report. NASA CR-134345, 1974.

6. Stone, Howard W.: The Leading-Edge Effects on the Laminar Flat-Plate Boundary Layer and the Aerodynamic Heating at Mach 10.4. NASA TN D-5160, 1969.

7. Bushnell, Dennis M.; Johnson, Charles B.; Harvey, William D.; and Feller, William V.: Comparison of Prediction Methods and Studies of Relaxation in Hypersonic Turbulent Nozzle-Wall Boundary Layers. NASA TN D-5433, 1969.

8. Nicoll, K. M.: Use of Transient "Thin-Wall" Technique in Measuring Heat Transfer Rates in Hypersonic Separated Flows. AIAA J., vol. 1, no. 4, Apr. 1963, pp. 940-941.

9. Dunavant, James C.; and Throckmorton, David A.: Aerodynamic Heat Transfer to RSI Tile Surfaces and Gap Intersections. J. Spacecraft & Rockets, vol. 11, no. 6, June 1974, pp. 437-440.

10. Marconi, Frank; Yaeger, Larry; and Hamilton, H. Harris: Computation of High-Speed Inviscid Flows About Real Configurations. Aerodynamic Analyses Requiring Advanced Computers, Part II, NASA SP-347, 1975, pp. 1411-1455.

TABLE I.- THERMOCOUPLE AND PRESSURE ORIFICE LOCATIONS

[Dimensions are in centimeters]

Thermocouple	x	y	z_{surf}	d
1	-27.00	0	1.38	---
2	-27.00	2.54	1.35	---
3	-27.00	5.08	1.26	---
4	-32.06	0	.94	---
5	-29.53	↓	1.16	---
6	-24.47	↓	1.61	---
7	-21.94	↓	1.83	---
8	-11.82	2.54	2.68	---
9	-11.81	5.08	2.59	---
10	-11.79	7.62	2.43	---
11	-11.77	10.16	2.21	---
12	-11.75	12.70	1.92	---
13	-16.85	7.62	1.99	---
14	-14.32	↓	2.21	---
15	-9.26	↓	2.65	---
16	-6.73	↓	2.87	---
17	3.36	0	4.04	---
18	3.37	2.54	4.01	---
19	3.37	5.08	3.91	---
20	-1.70	0	3.60	---
21	.83	↓	3.82	---
22	5.89	↓	4.26	---
23	8.42	↓	4.48	---
24	3.41	10.16	3.54	---
25	3.43	12.70	3.25	---
26	3.46	15.24	2.90	---
27	3.50	17.78	2.49	---
28	3.54	20.32	2.01	---
29	-1.60	15.24	2.46	---
30	.93	↓	2.68	---
31	5.99	↓	3.12	---
32	8.52	↓	3.35	---
33	-3.44	11.43	2.80	---
34	-4.01	11.43	2.75	0
35	-4.01	11.43	---	.57
36	-15.61	1.87	2.36	---
37	↓	1.30	2.37	---
38	↓	.73	2.38	---
39	↓	.16	2.38	0
40	↓	.16	---	.57
41	↓	.16	---	1.14
42	-8.02	1.87	3.08	---

Thermocouple	x	y	z_{surf}	d
43	-8.02	1.30	3.04	---
44	↓	.73	3.04	---
45	↓	.16	3.04	0
46	↓	.16	---	.57
47	↓	.16	---	1.14
48	-2.35	3.81	3.47	---
49	-2.93	↓	3.42	---
50	-3.50	↓	3.37	---
51	-4.06	↓	3.32	0
52	↓	↓	---	.57
53	↓	↓	---	1.14
54	↓	↓	---	1.71
55	↓	↓	---	2.29
56	-4.22	↓	---	2.86
57	-2.36	0	3.54	---
58	-2.93	↓	3.49	---
59	-3.50	↓	3.44	---
60	-4.07	↓	3.39	0
61	↓	↓	---	.57
62	↓	↓	---	1.14
63	↓	↓	---	1.71
64	↓	↓	---	2.29
65	-4.23	↓	---	2.86
66	-4.07	1.14	---	.57
67	-4.07	.57	---	.57

Pressure orifice	x	y	z_{surf}	d
1	-11.82	-2.54	2.68	---
2	-11.81	-5.08	2.59	---
3	-11.79	-7.62	2.43	---
4	-11.77	-10.16	2.21	---
5	-11.75	-12.70	1.92	---
6	-14.32	-7.62	2.21	---
7	-9.26	-7.62	2.65	---
8	-4.22	-3.81	---	2.86
9	-4.20	-7.62	---	↓
10	-4.17	-11.43	---	↓
11	-4.13	-15.24	---	↓
12	-4.07	-19.05	---	↓

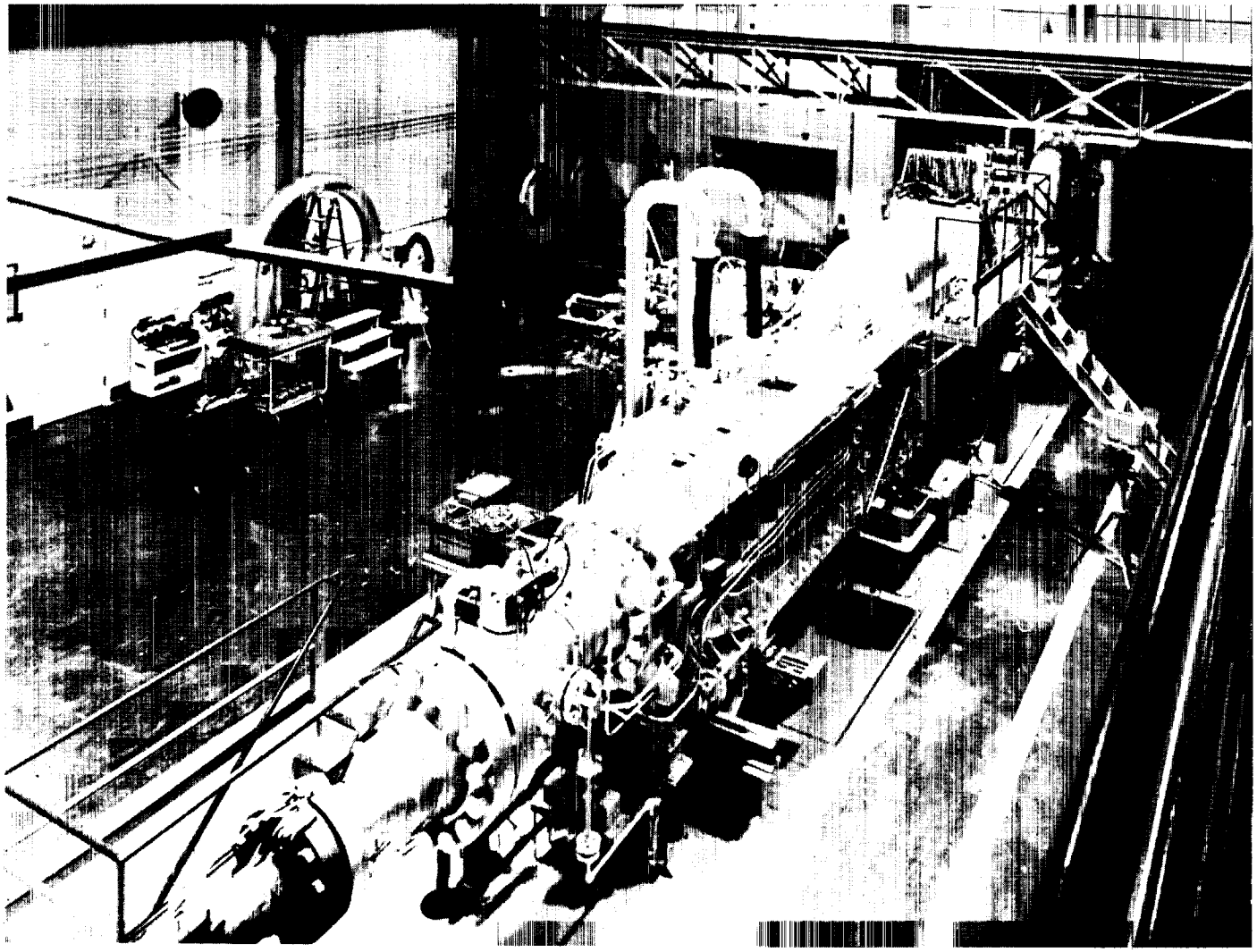

L-74-2970

Figure 1.- Langley continuous flow hypersonic tunnel.

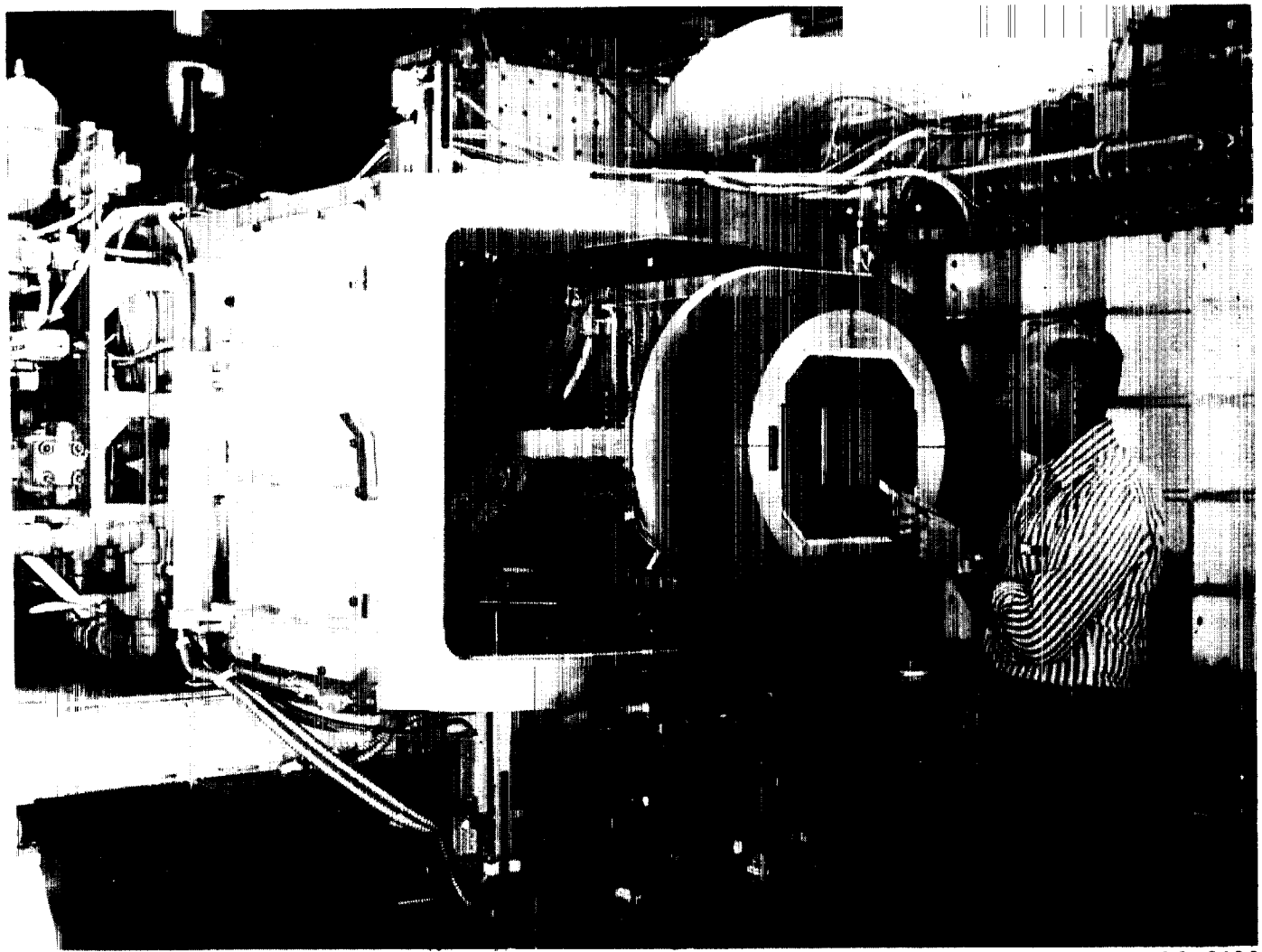

L-73-2830

(a) Model access position.

Figure 2.- Model injection mechanism.

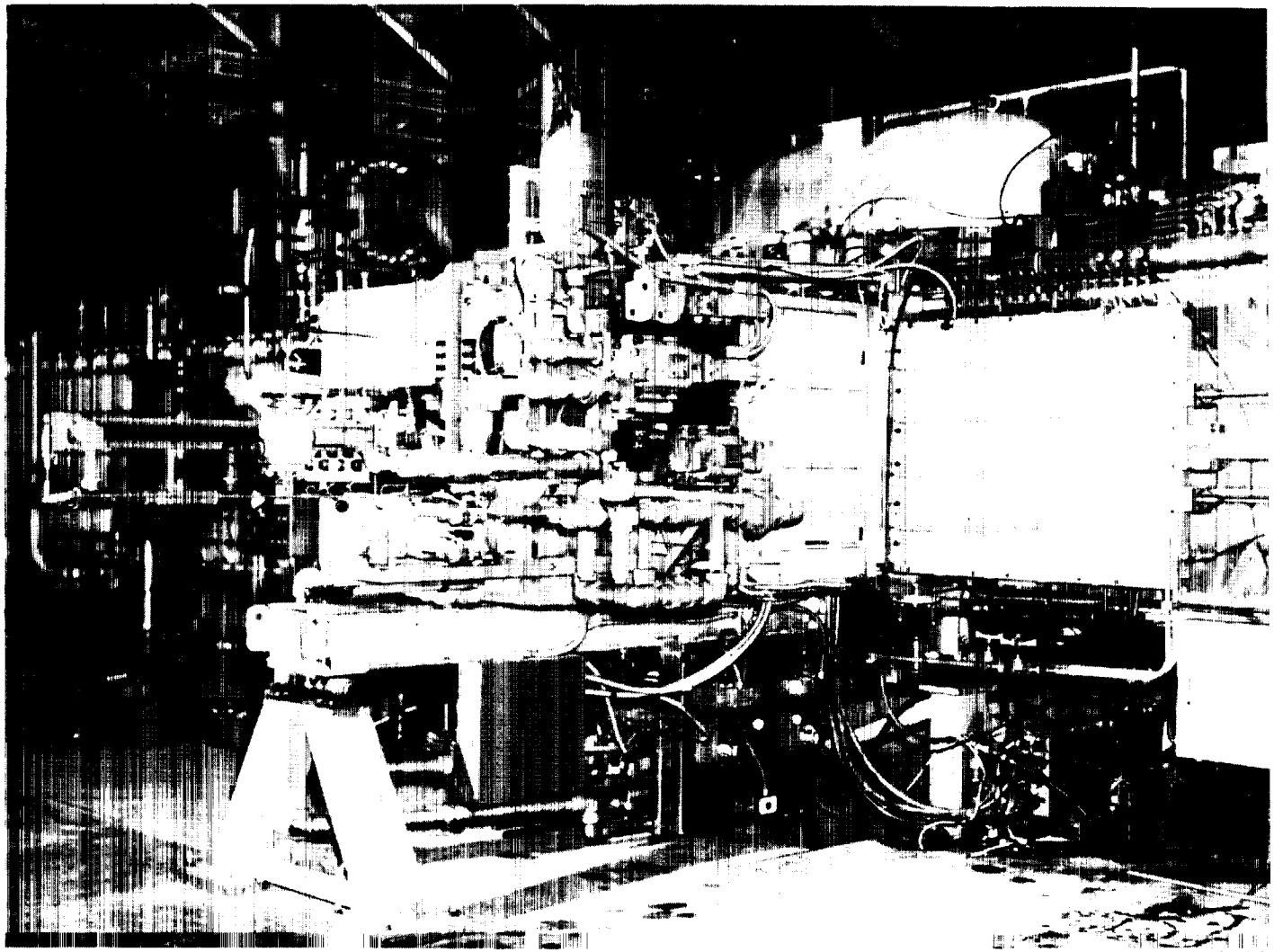

L-73-2333

(b) Rotated to test position.

Figure 2.- Concluded.

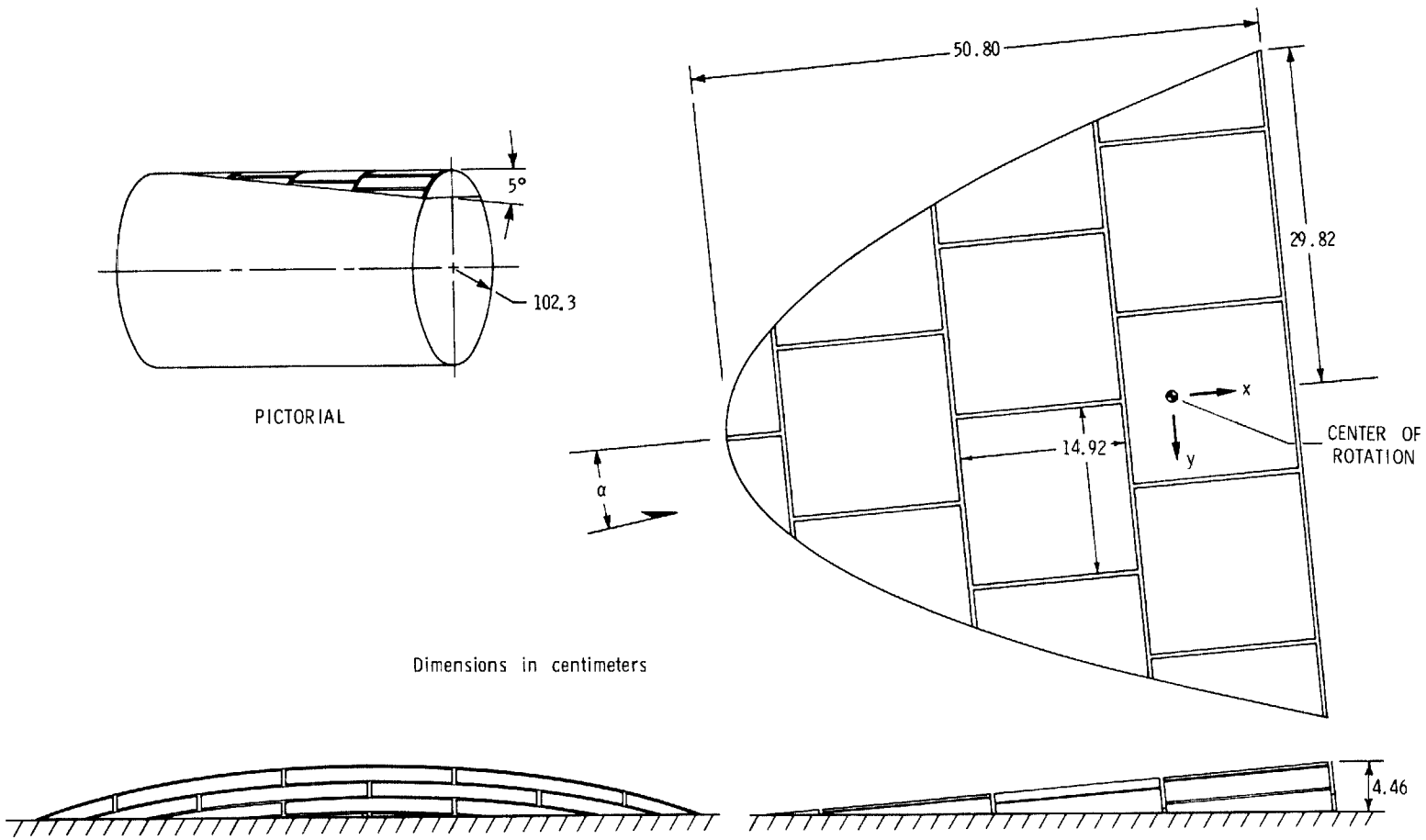

Figure 3.- Schematic drawing of the RSI pressure-gradient model.

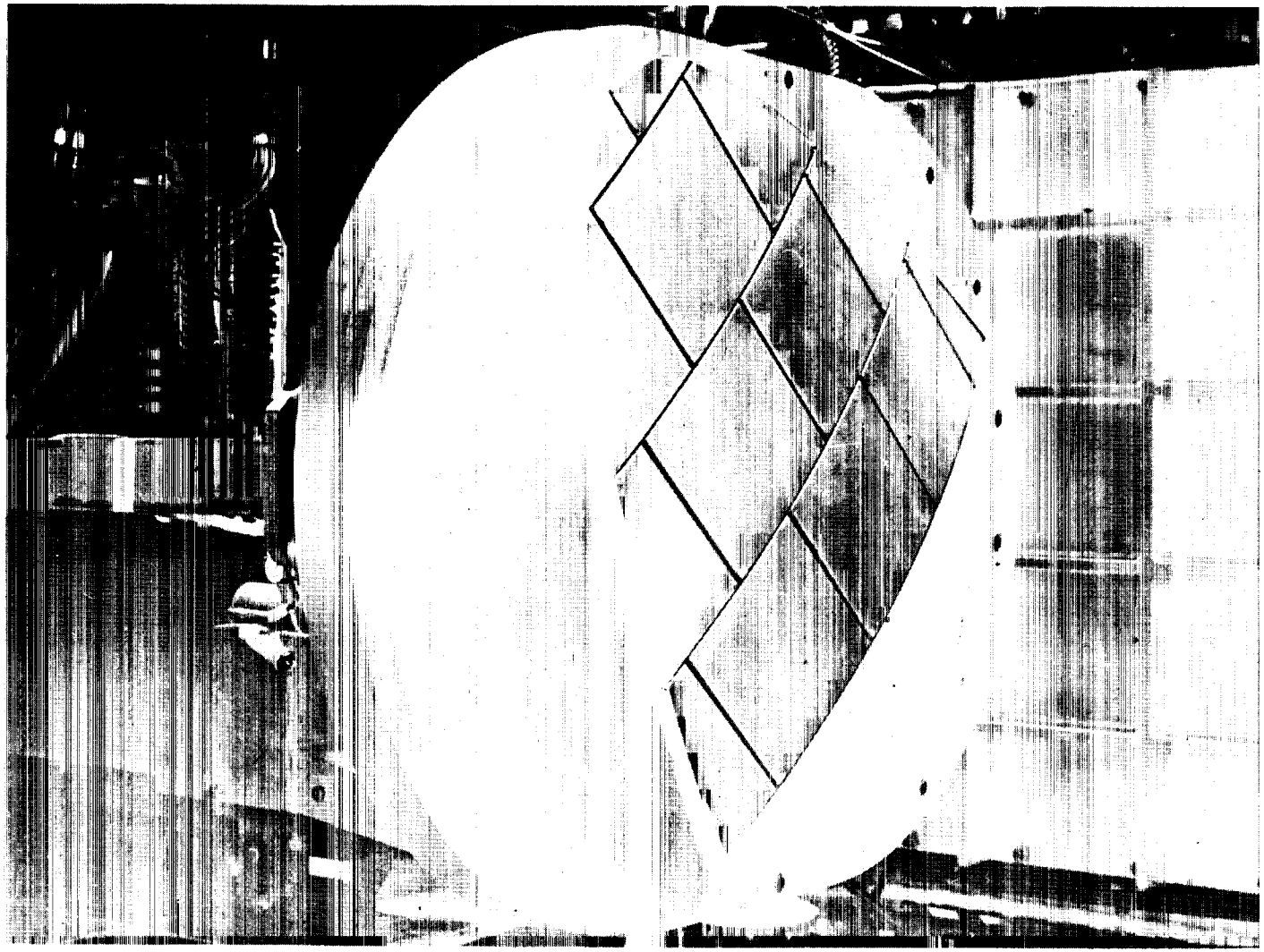

L-73-6244

(a) Model access position.

Figure 4.- RSI pressure-gradient model mounted on injection strut.

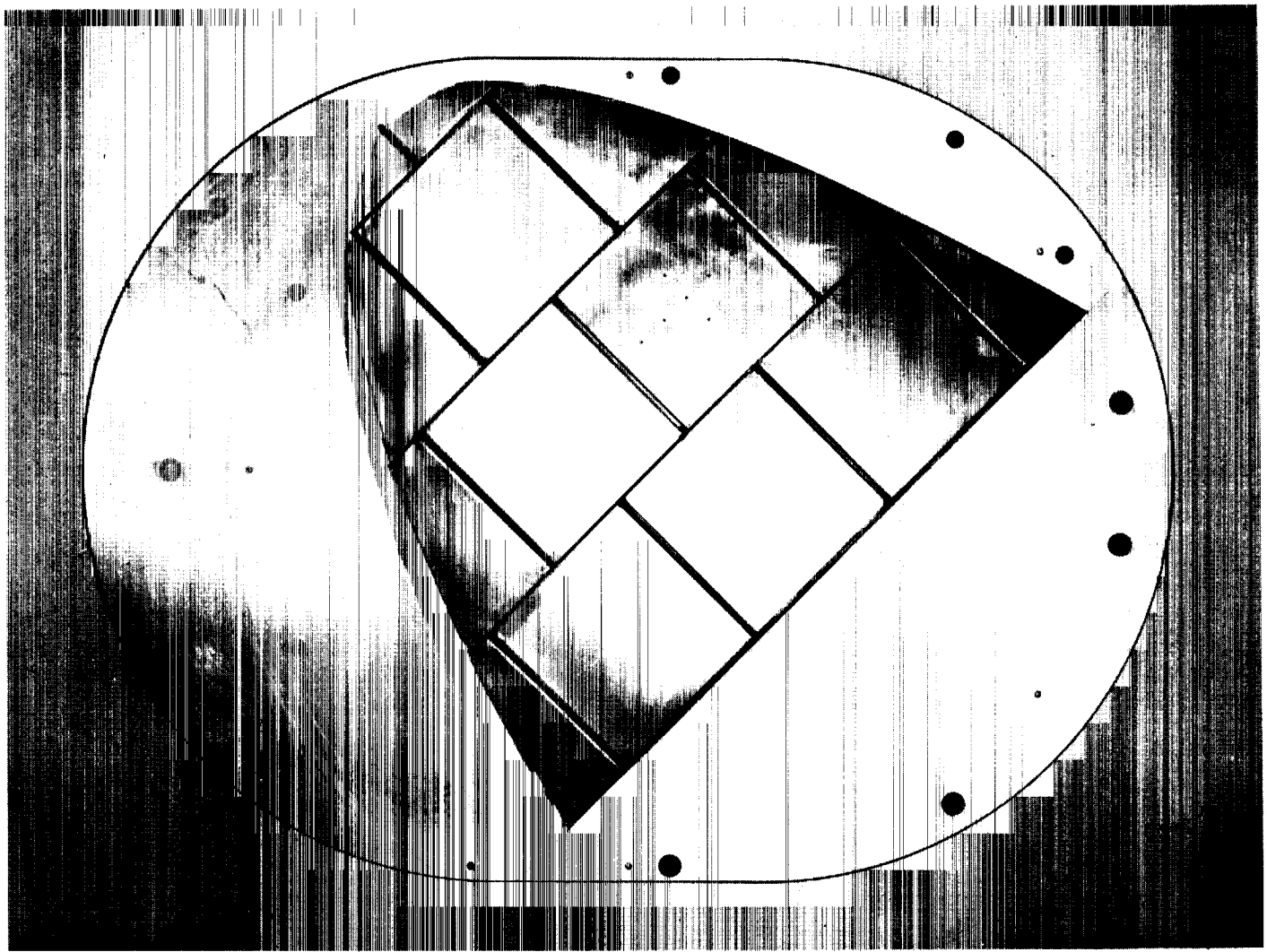

L-73-6243

(b) Model in test position.

Figure 4.- Concluded.

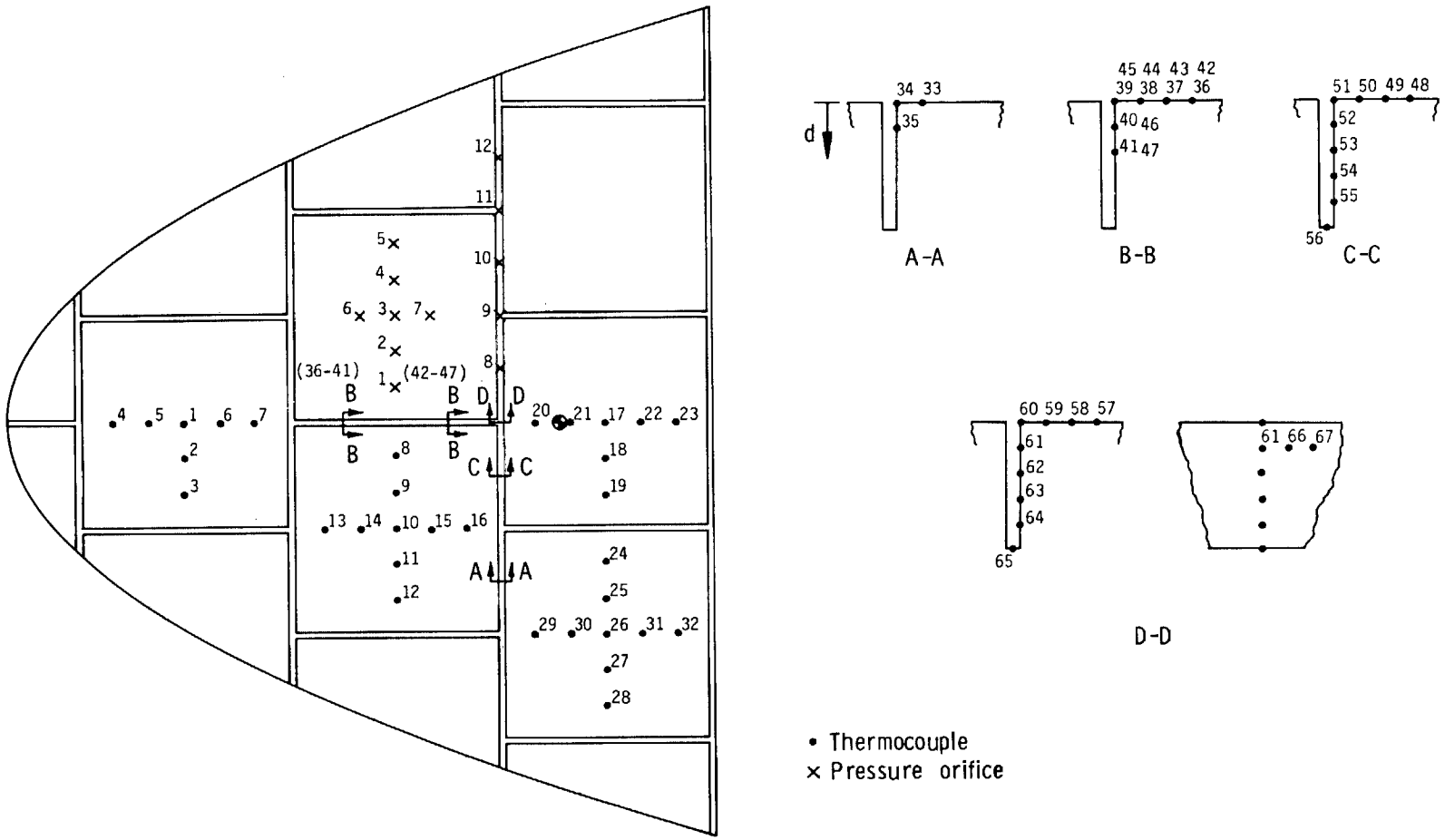

Figure 5.- RSI pressure-gradient model instrumentation locations.

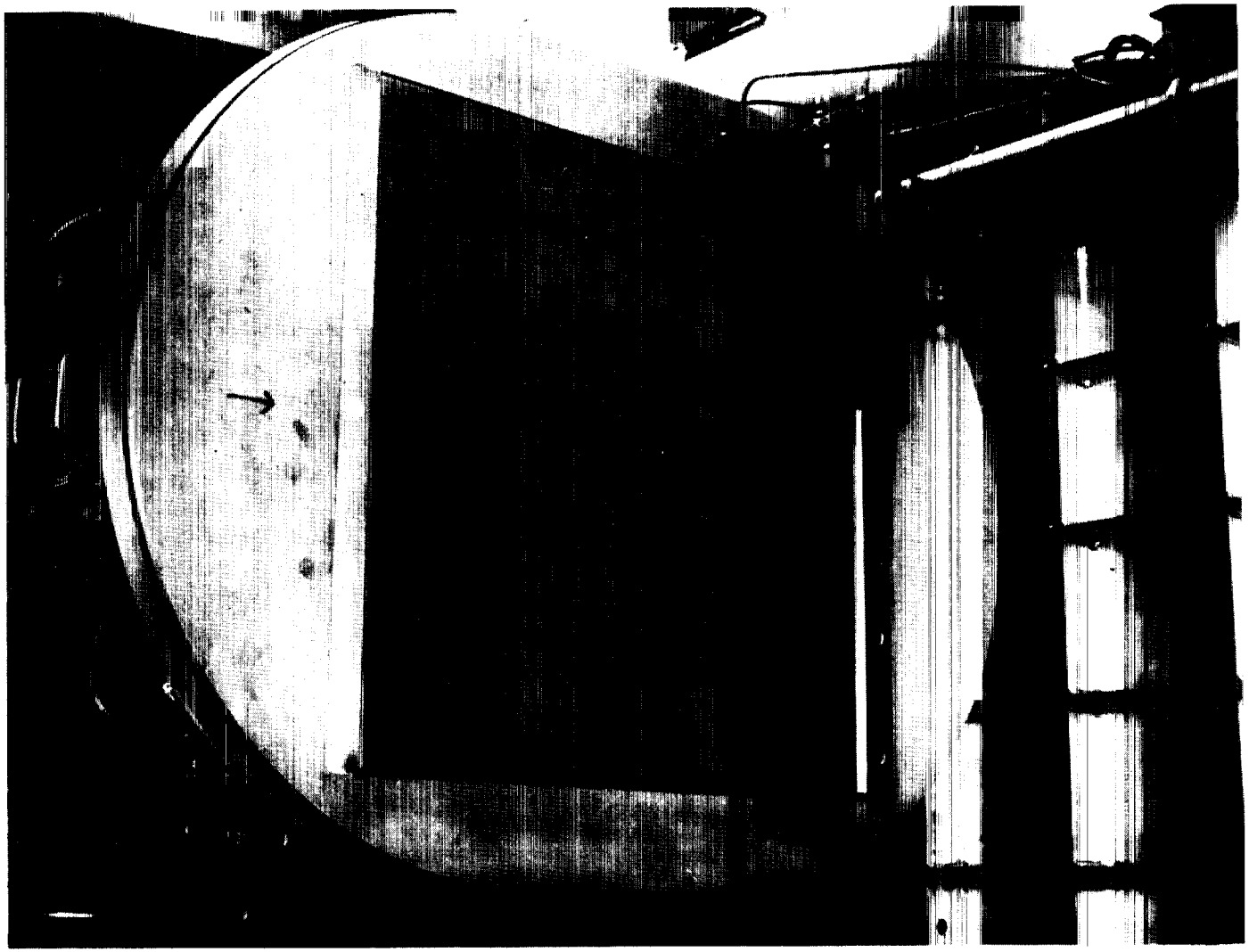

L-73-3763

Figure 6.- Flat-plate model mounted on injection strut.

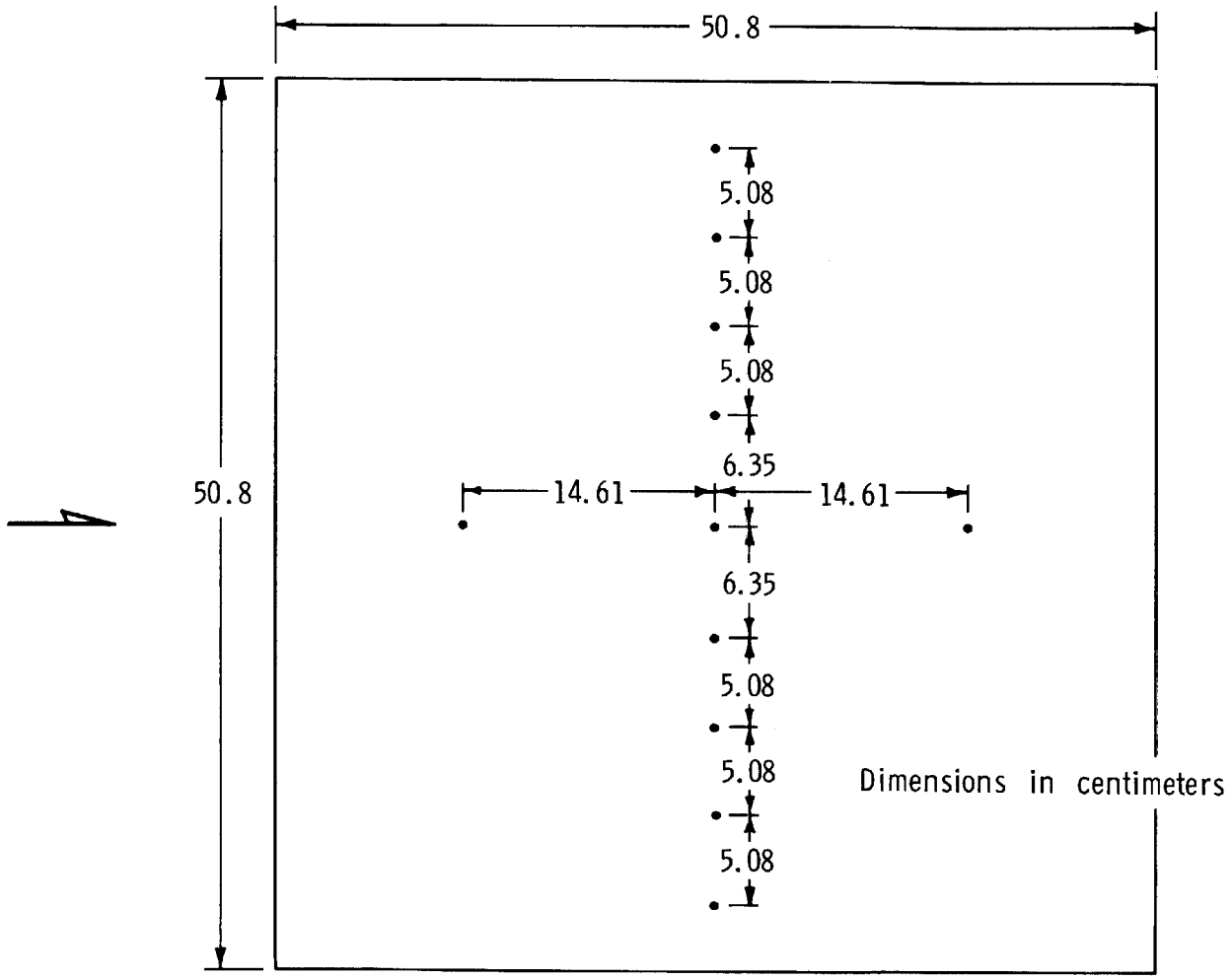

Figure 7.- Flat-plate model instrumentation locations.

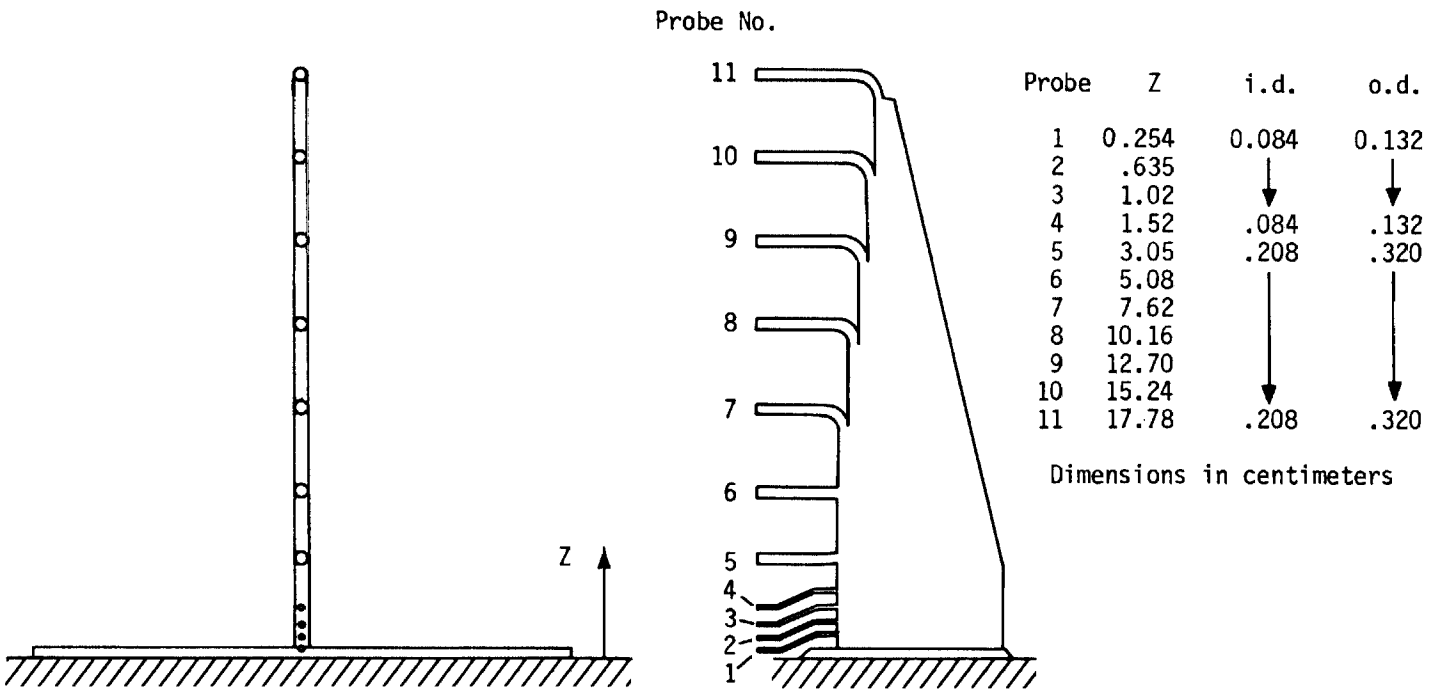

Figure 8.- Schematic drawing of boundary-layer pitot-probe rake.

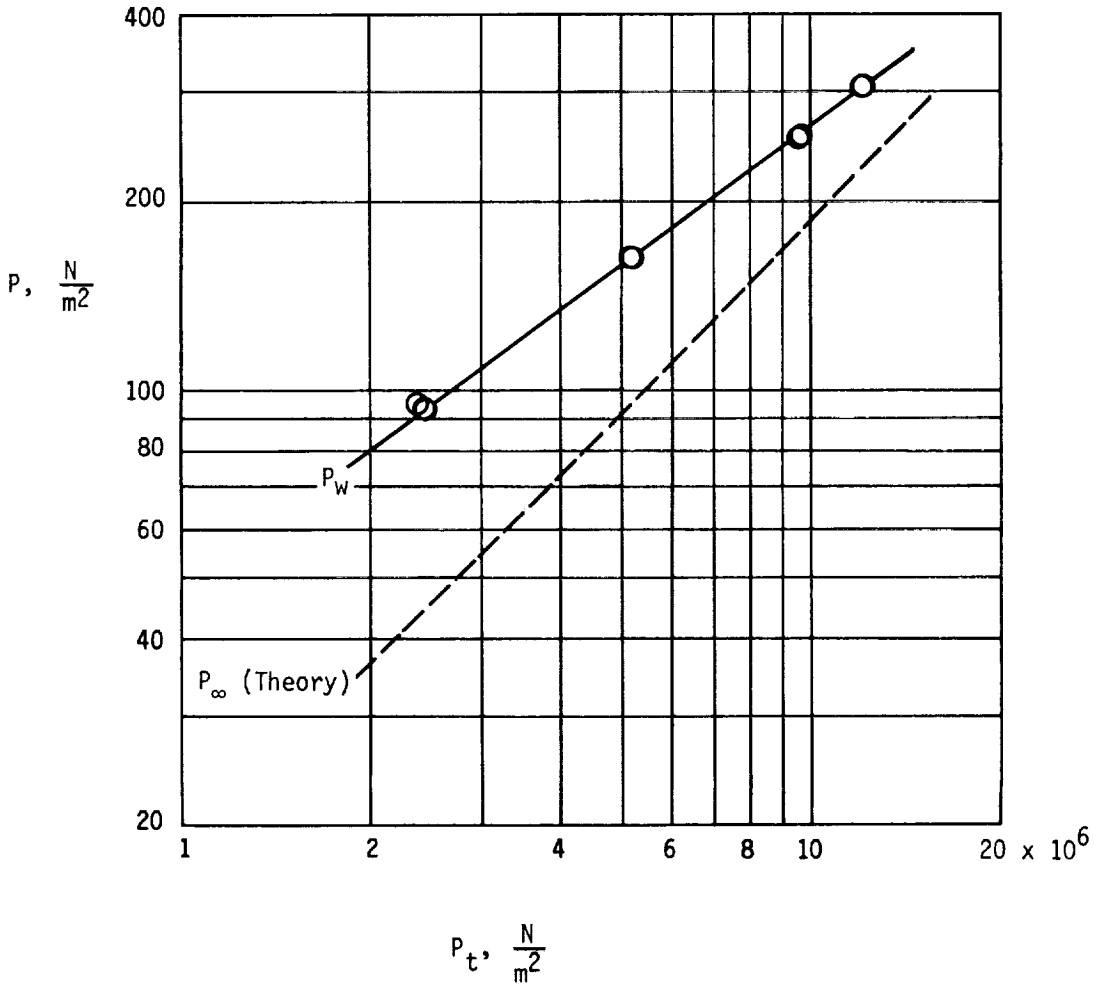

Figure 9.- Comparison of center-line wall and free-stream static pressures.

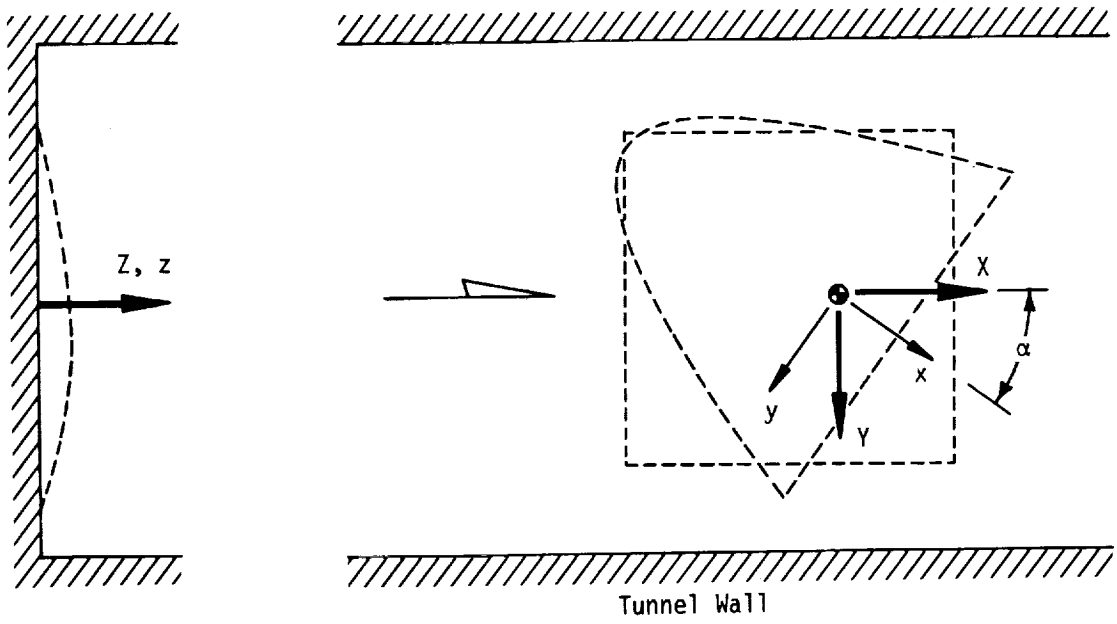

Figure 10.- Definition of coordinate systems.

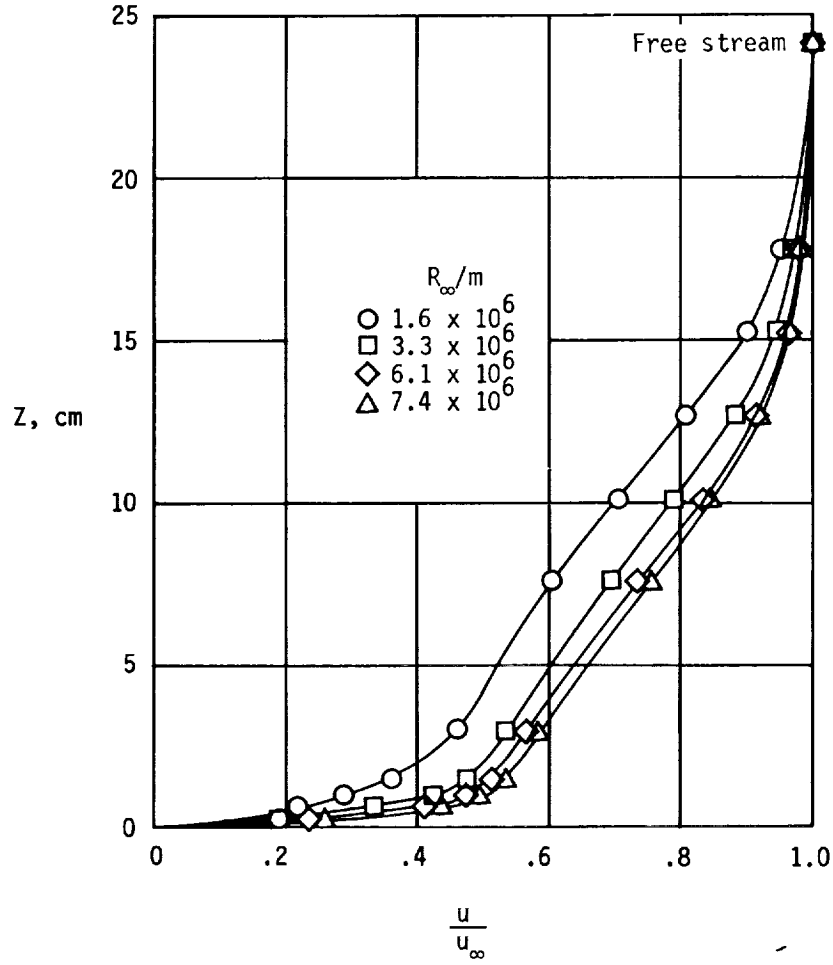

Figure 11.- Boundary-layer velocity profiles at sidewall center line. Y = 0.

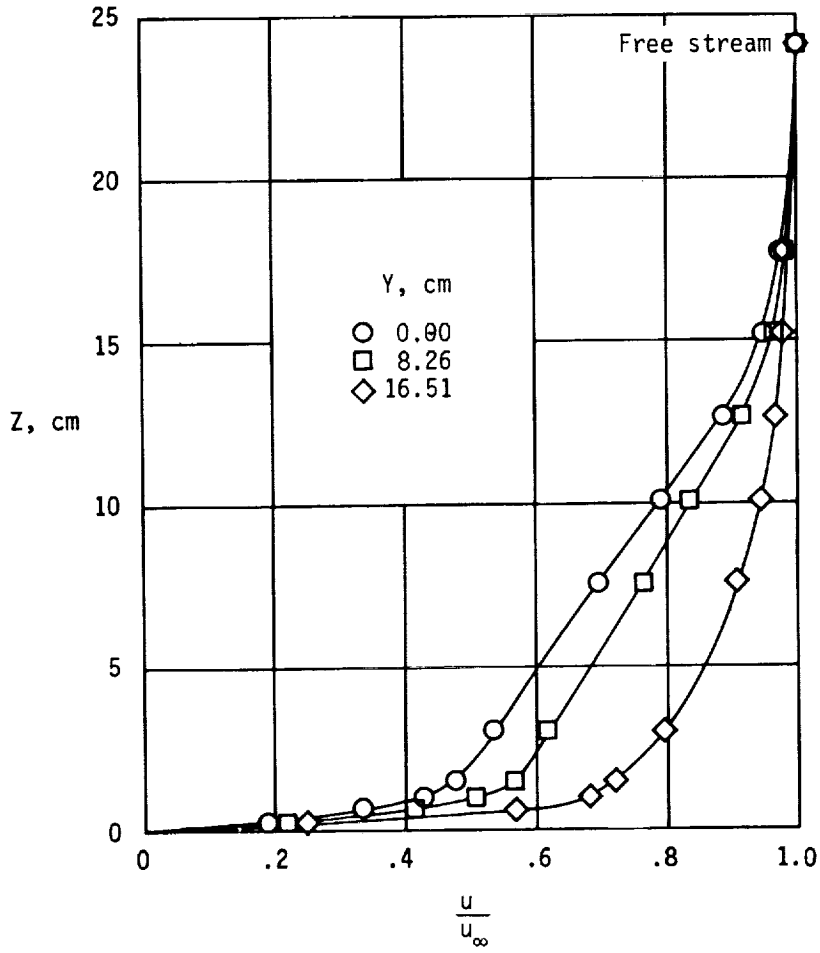

Figure 12.- Transverse variation of boundary-layer velocity profile. $R_\infty = 3.3 \times 10^6$ per meter.

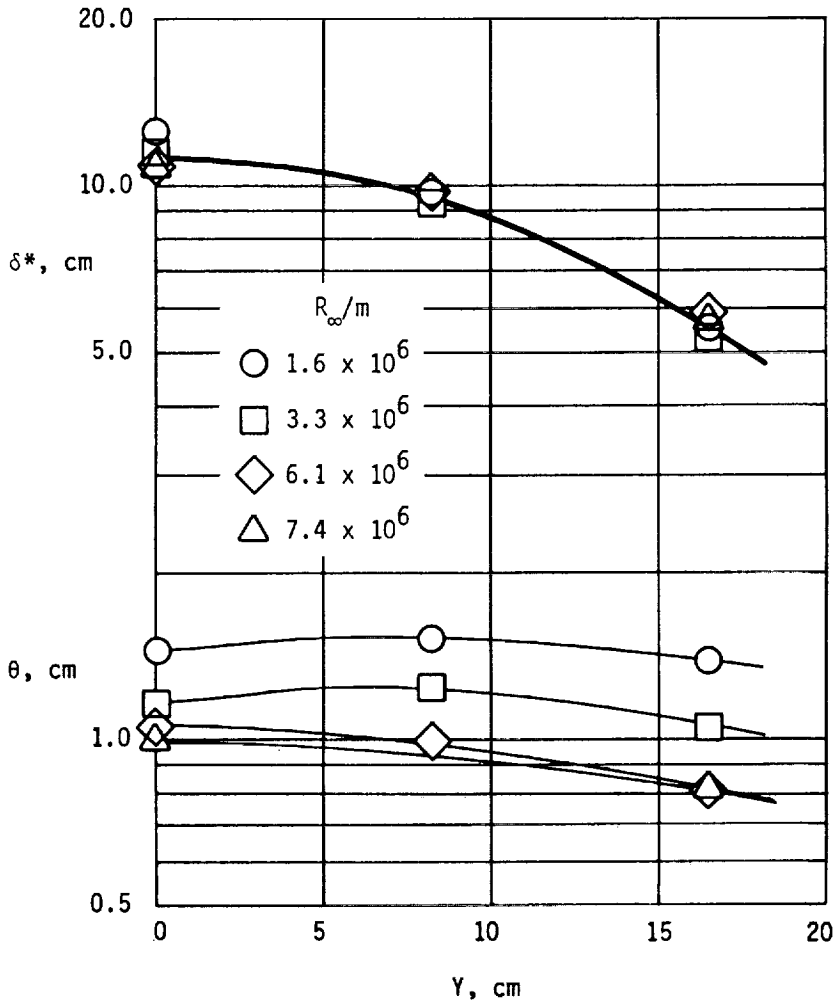

Figure 13.- Variation of displacement and momentum thicknesses with transverse wall position.

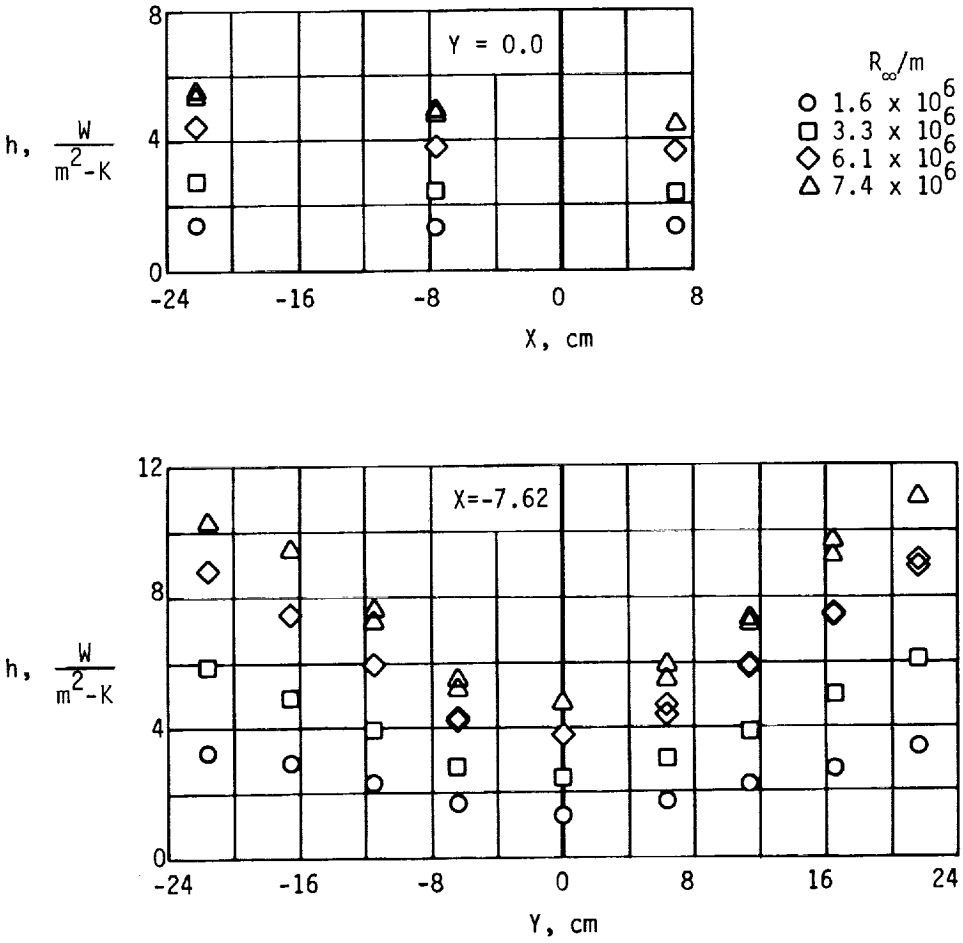

Figure 14.- Heat-transfer-coefficient distribution on the flat plate.

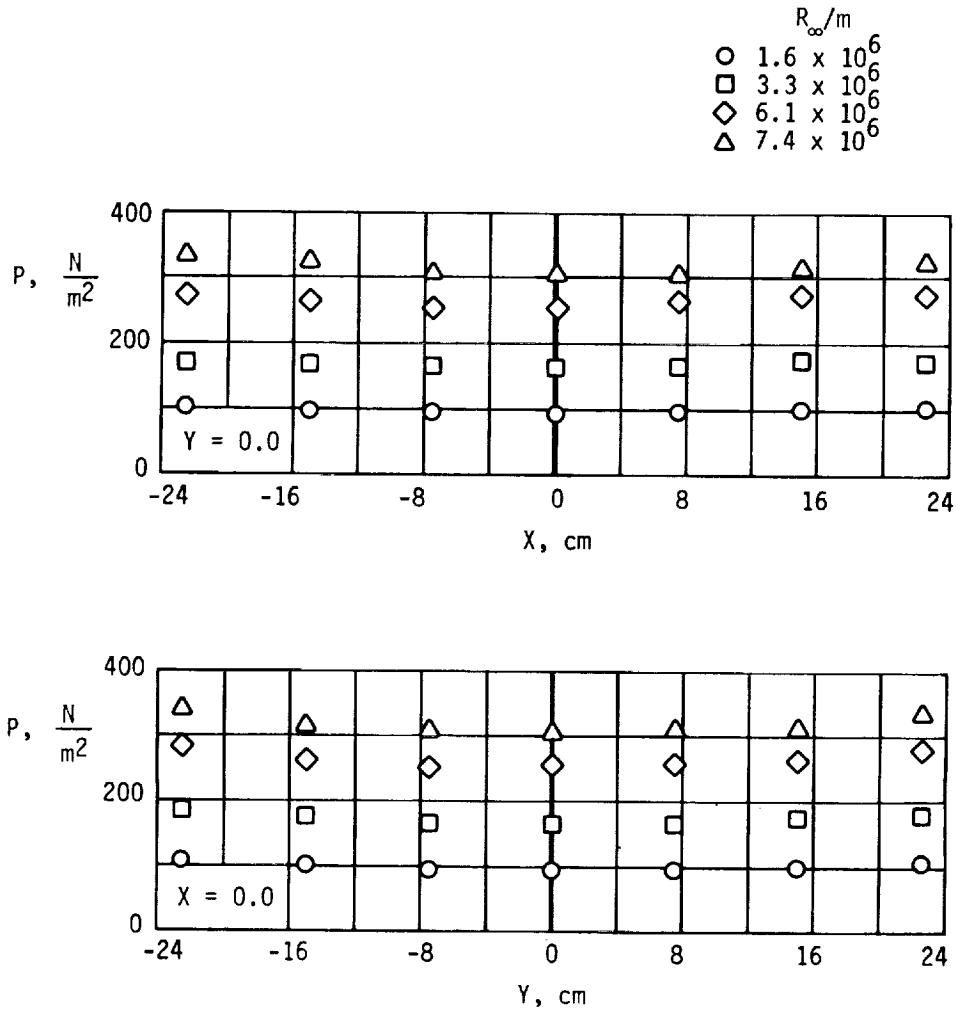

Figure 15.- Static pressure distribution on the flat plate.

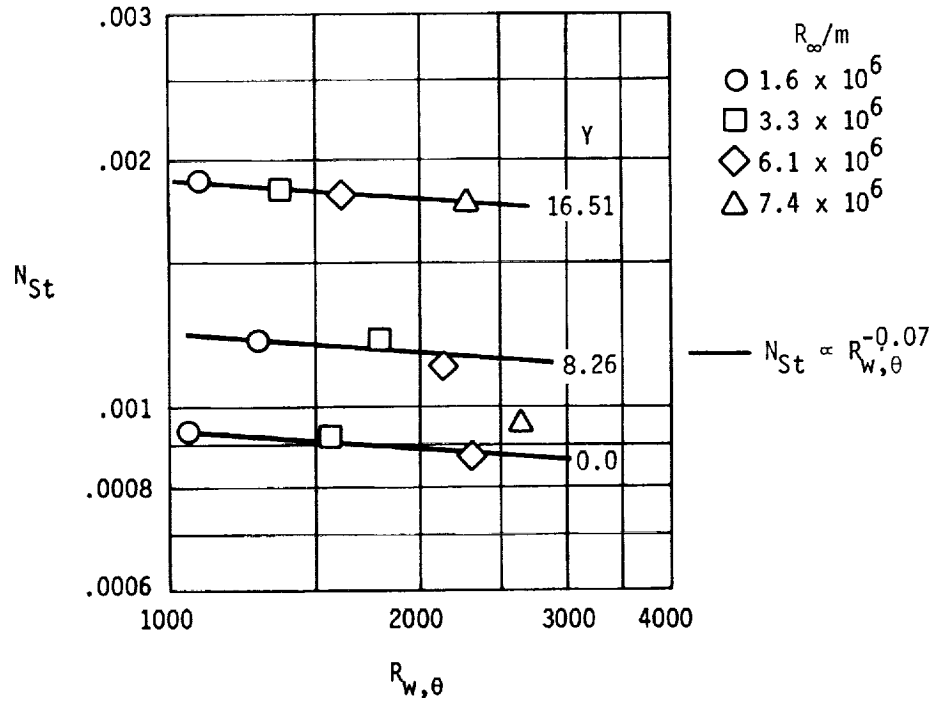

Figure 16.- Variation of flat-plate Stanton number with momentum-thickness Reynolds number.

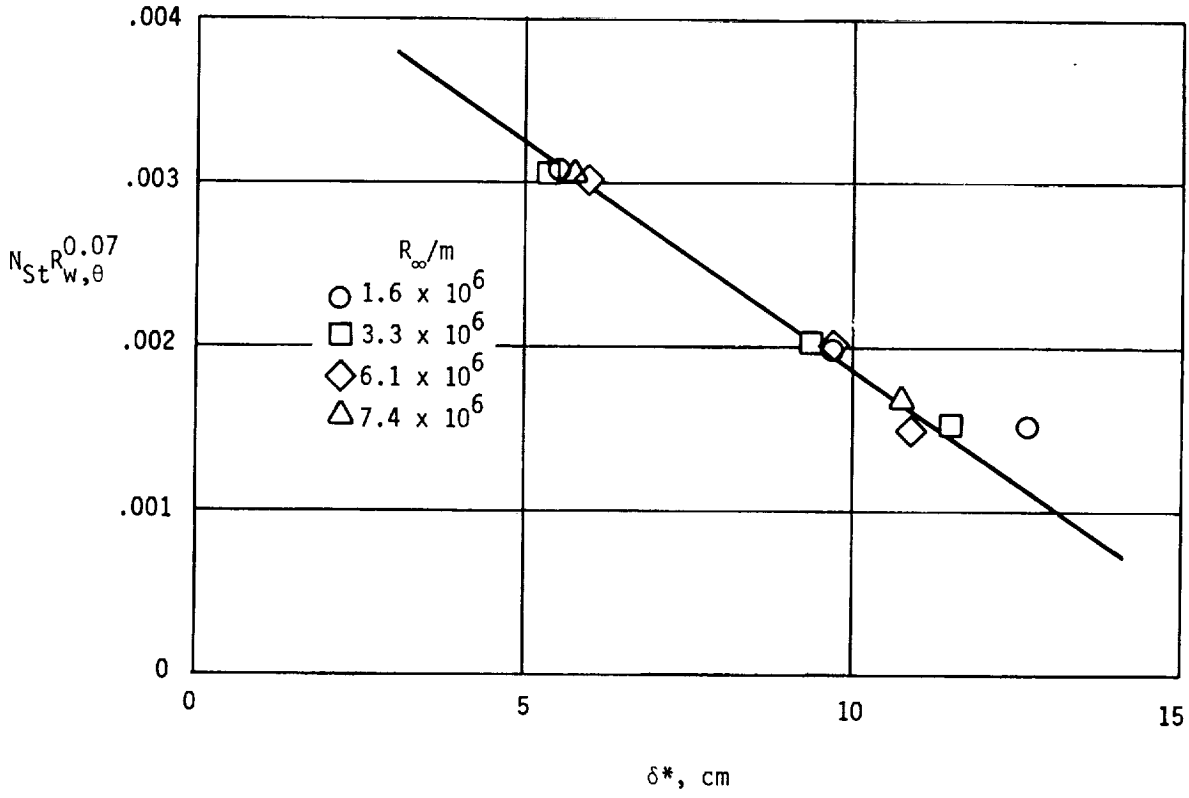

Figure 17.- Correlation of flat-plate heat transfer with displacement thickness.

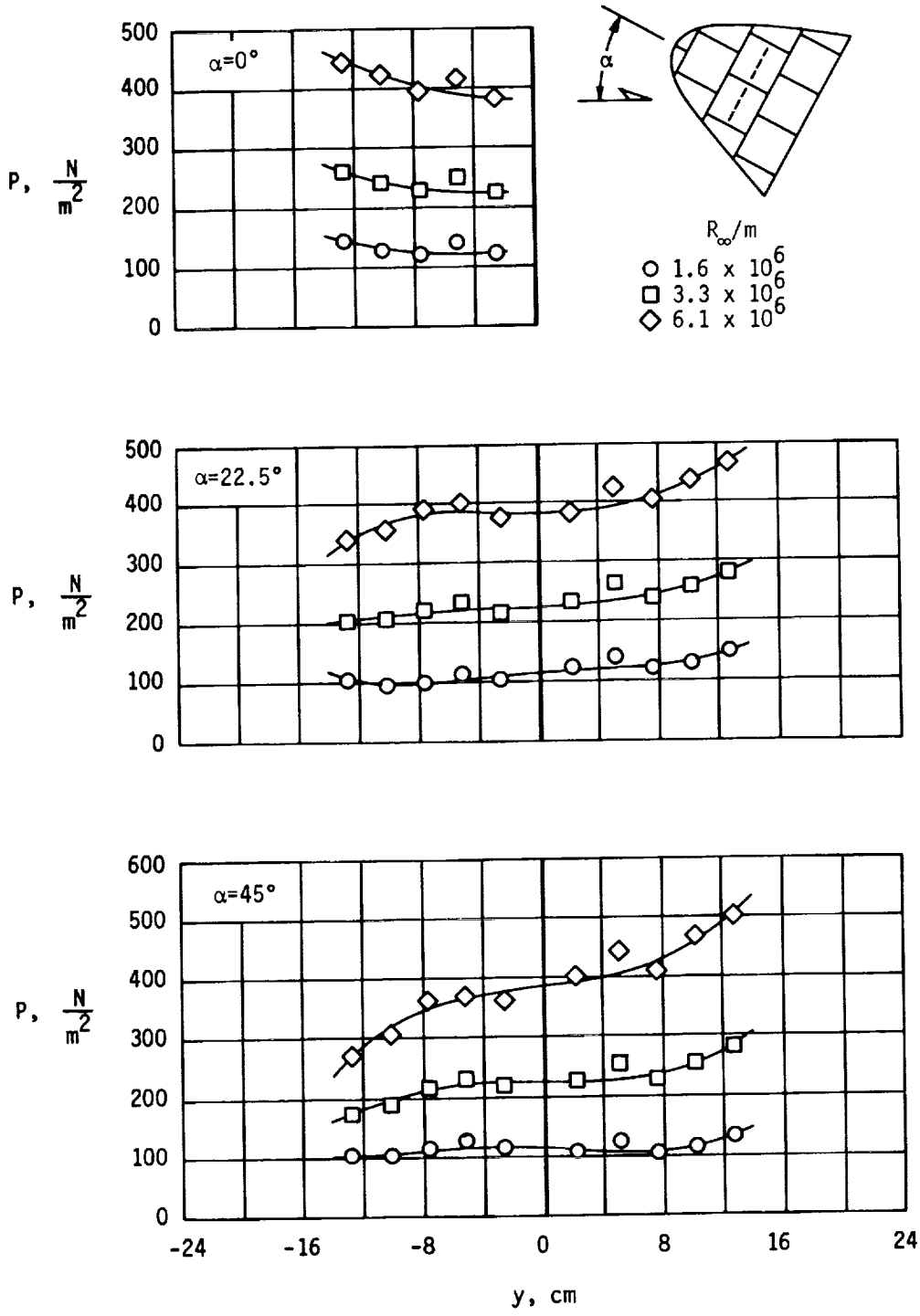

Figure 18.- Static pressure distributions on the smoothed RSI tile-array model.

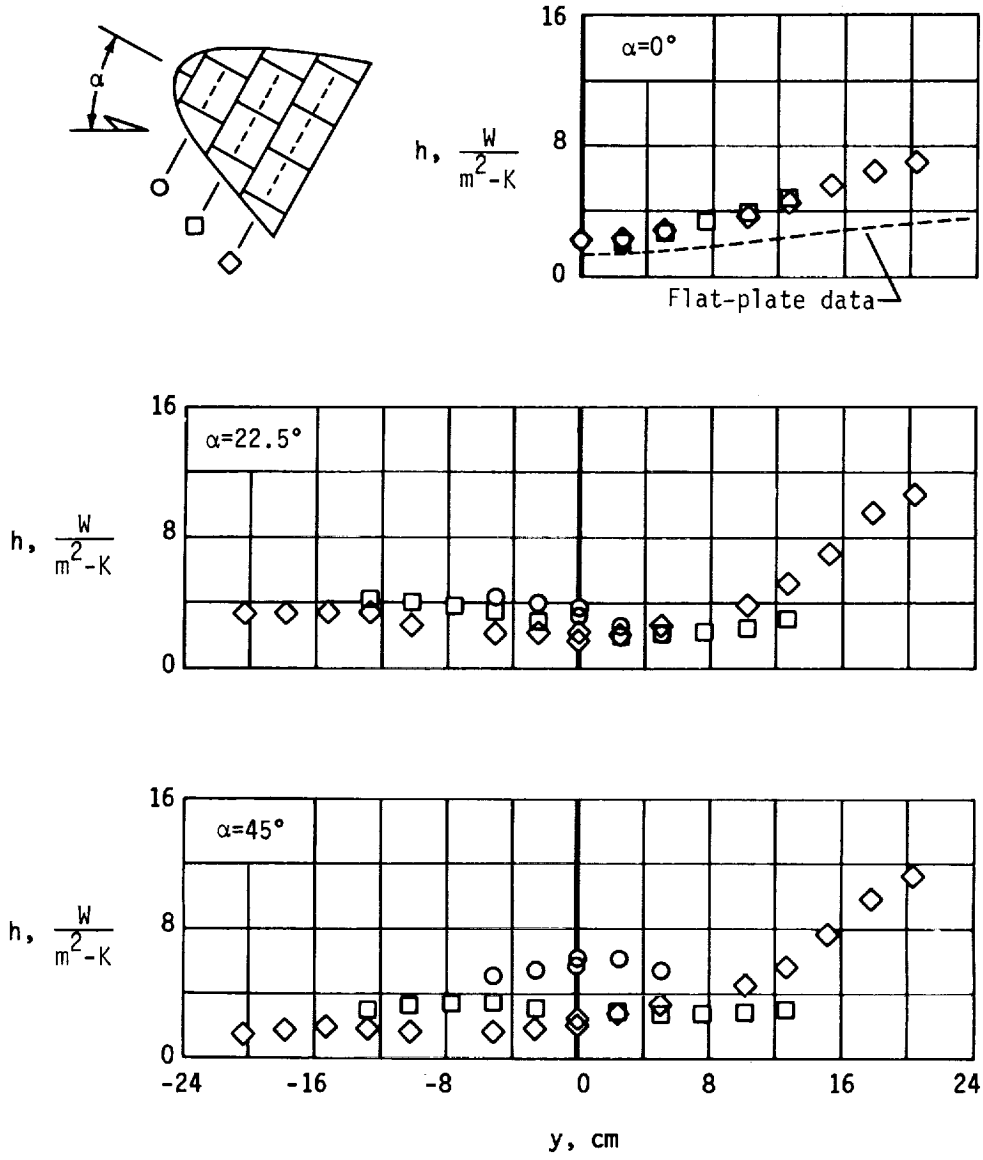

(a) $R_\infty = 1.6 \times 10^6$ per meter.

Figure 19.- Surface heat-transfer distributions on the smoothed RSI tile-array model.

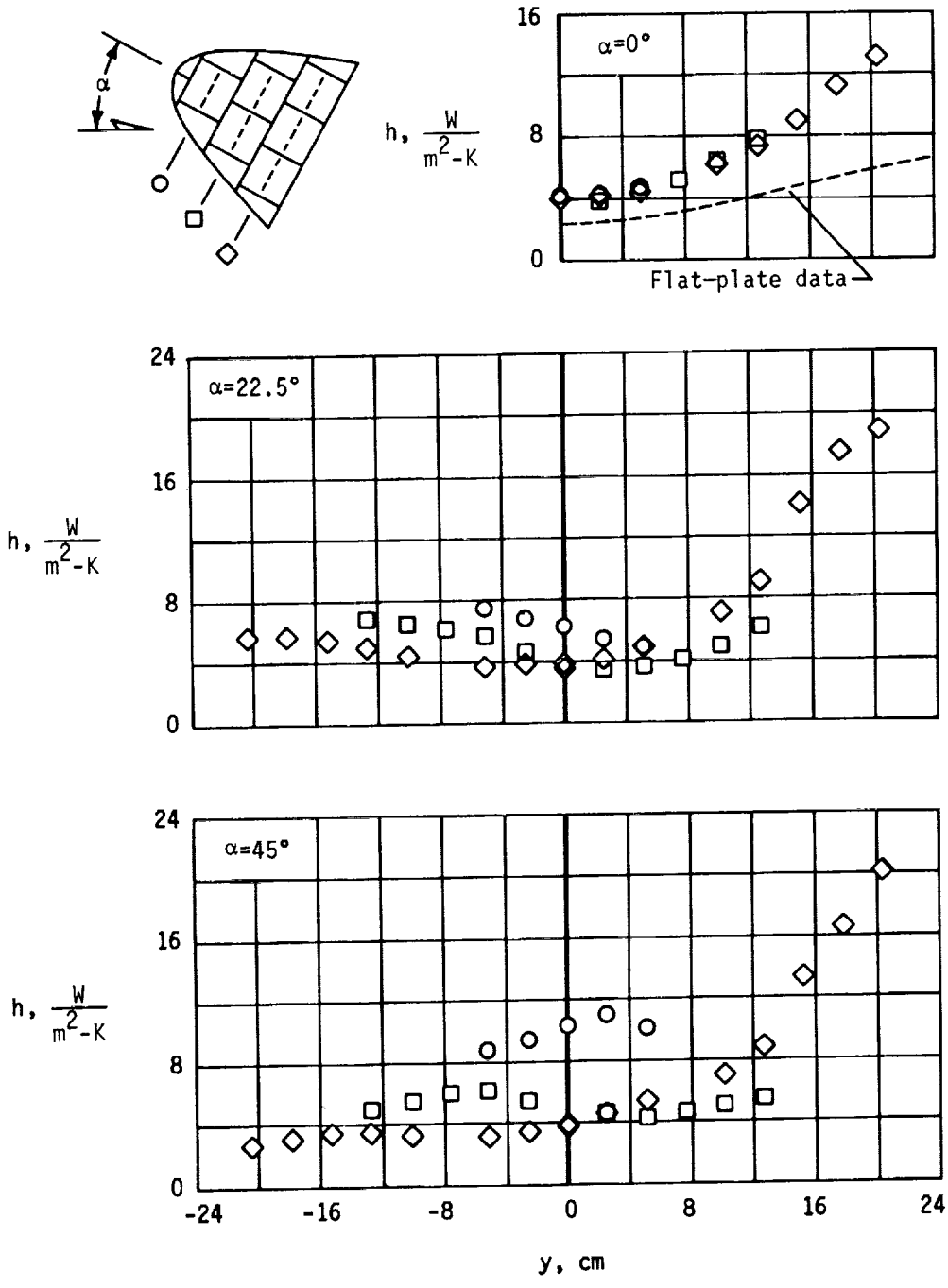

(b) $R_\infty = 3.3 \times 10^6$ per meter.

Figure 19.- Continued.

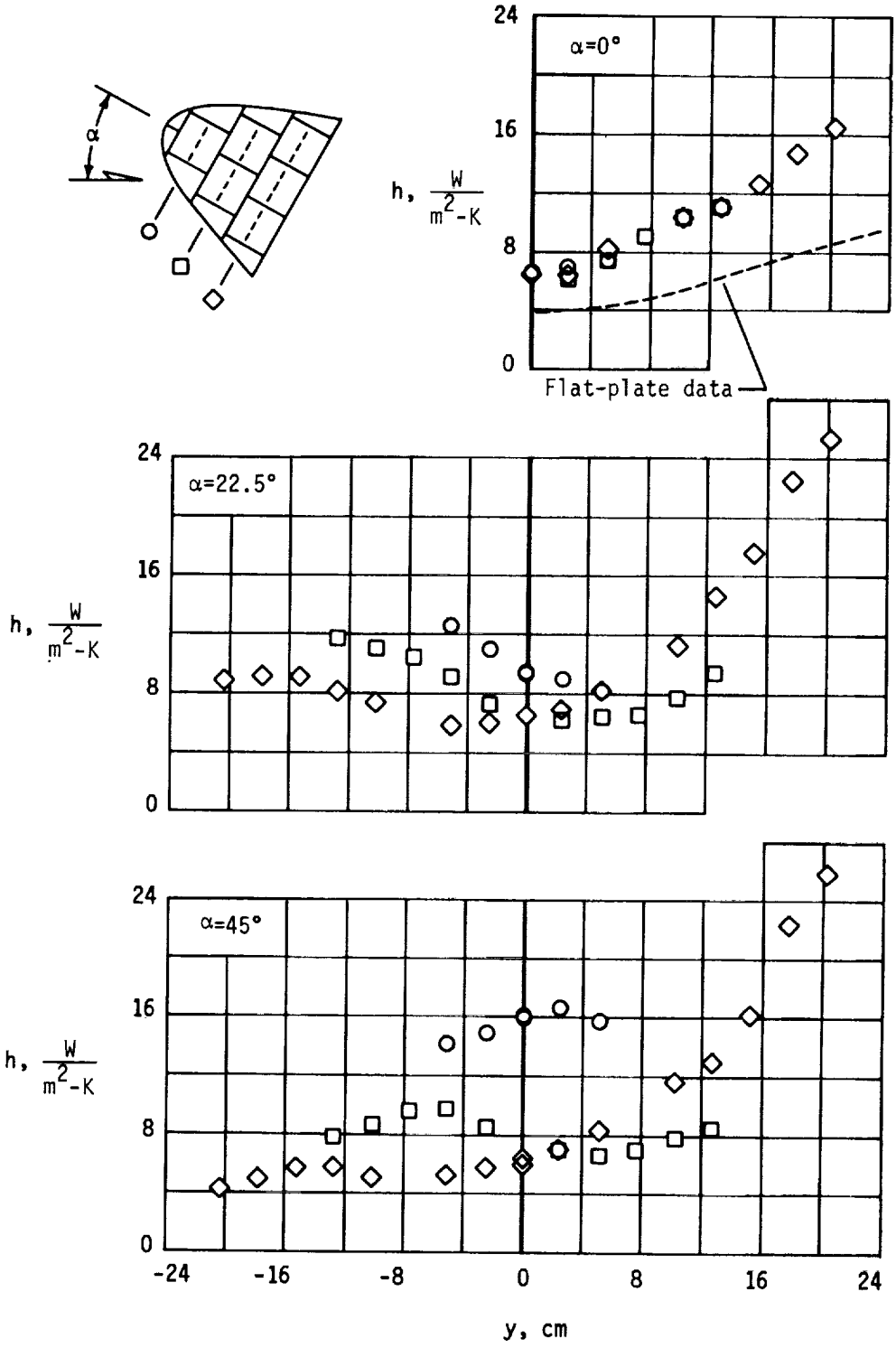

(c) $R_\infty = 6.1 \times 10^6$ per meter.

Figure 19.- Concluded.

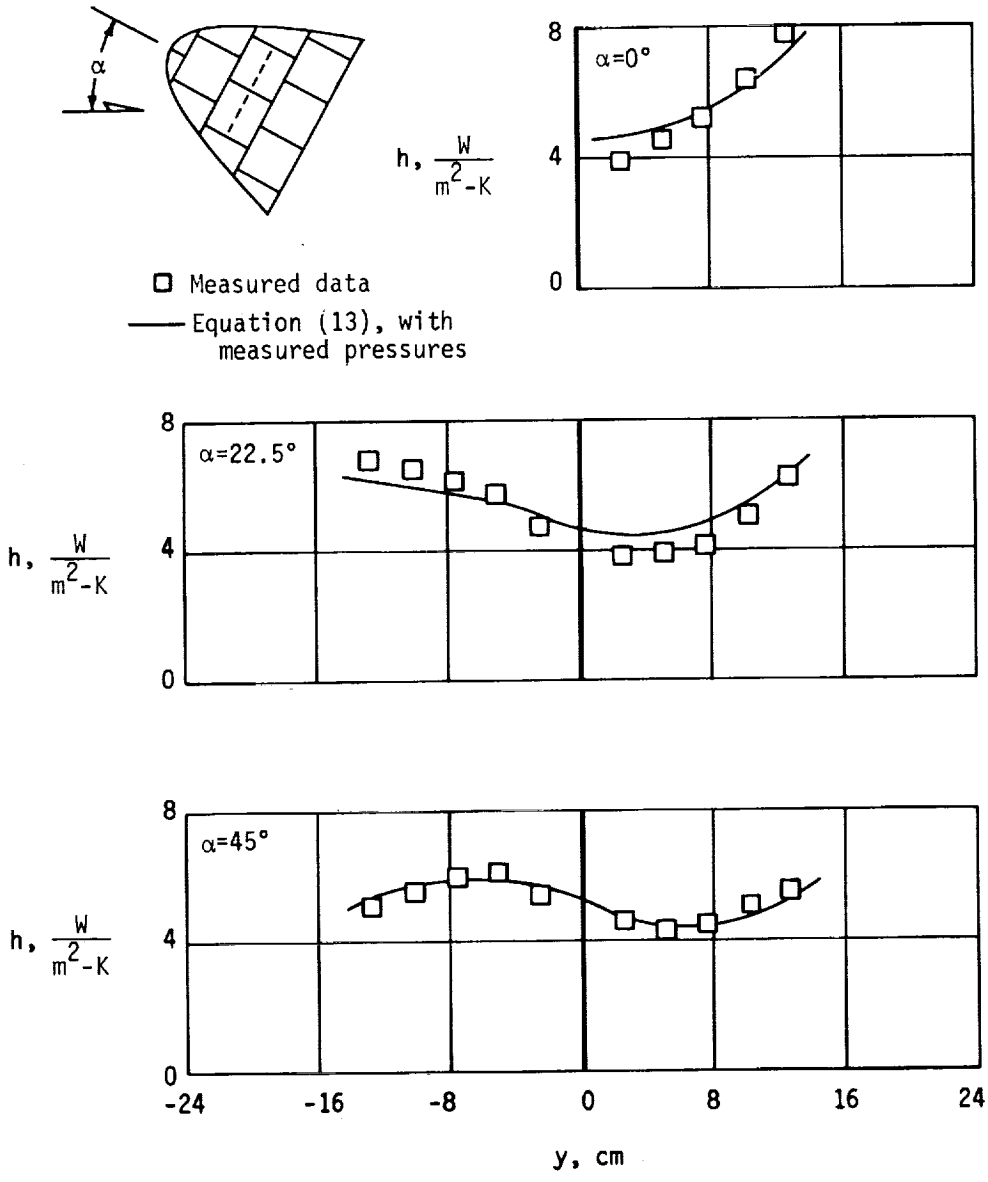

Figure 20.- Comparison of measured and predicted heat transfer to the smoothed RSI tile-array model using measured pressure data. $R_\infty = 3.3 \times 10^6$ per meter.

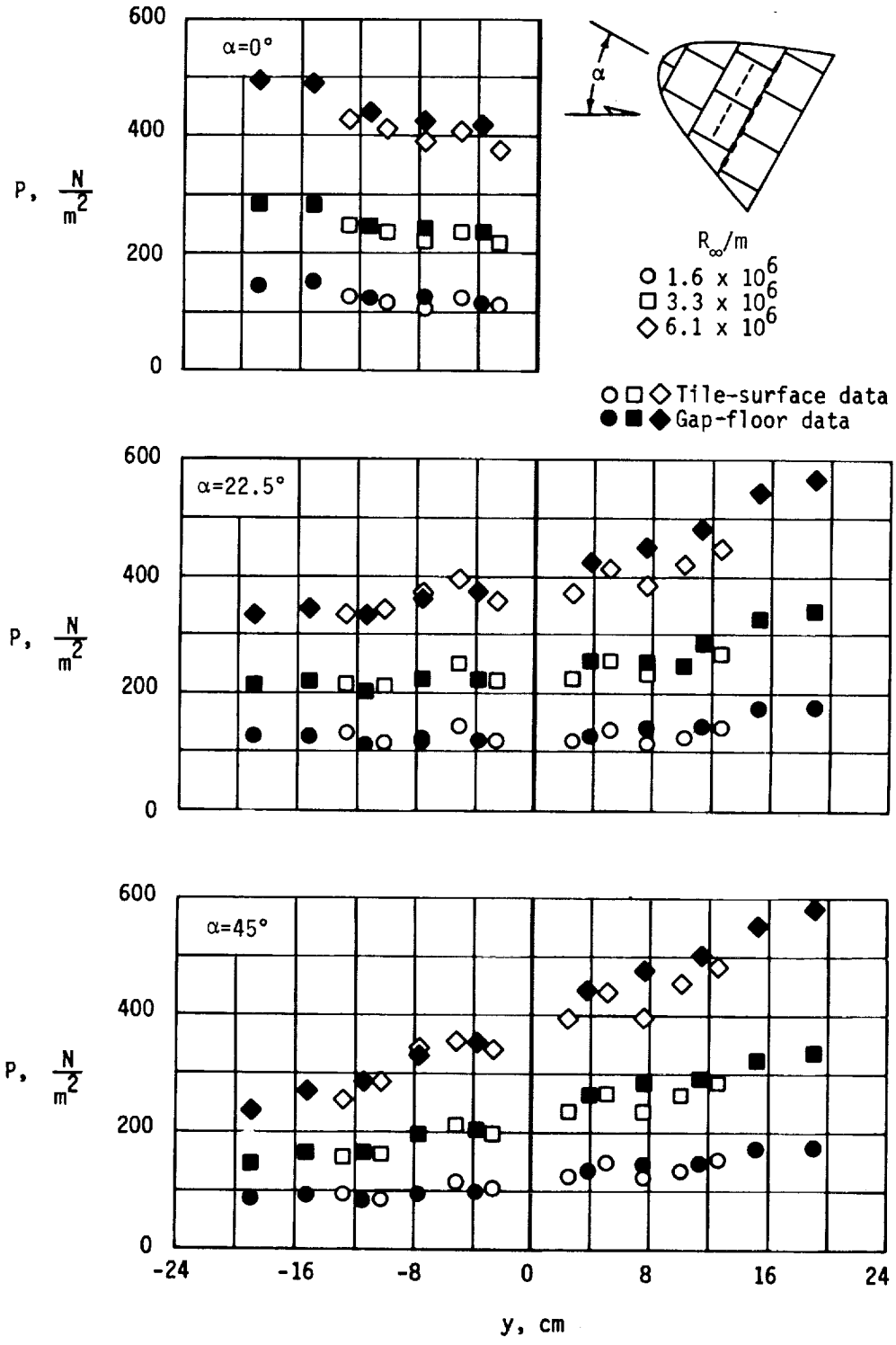

Figure 21.- Static pressure distributions on the RSI tile-array model.

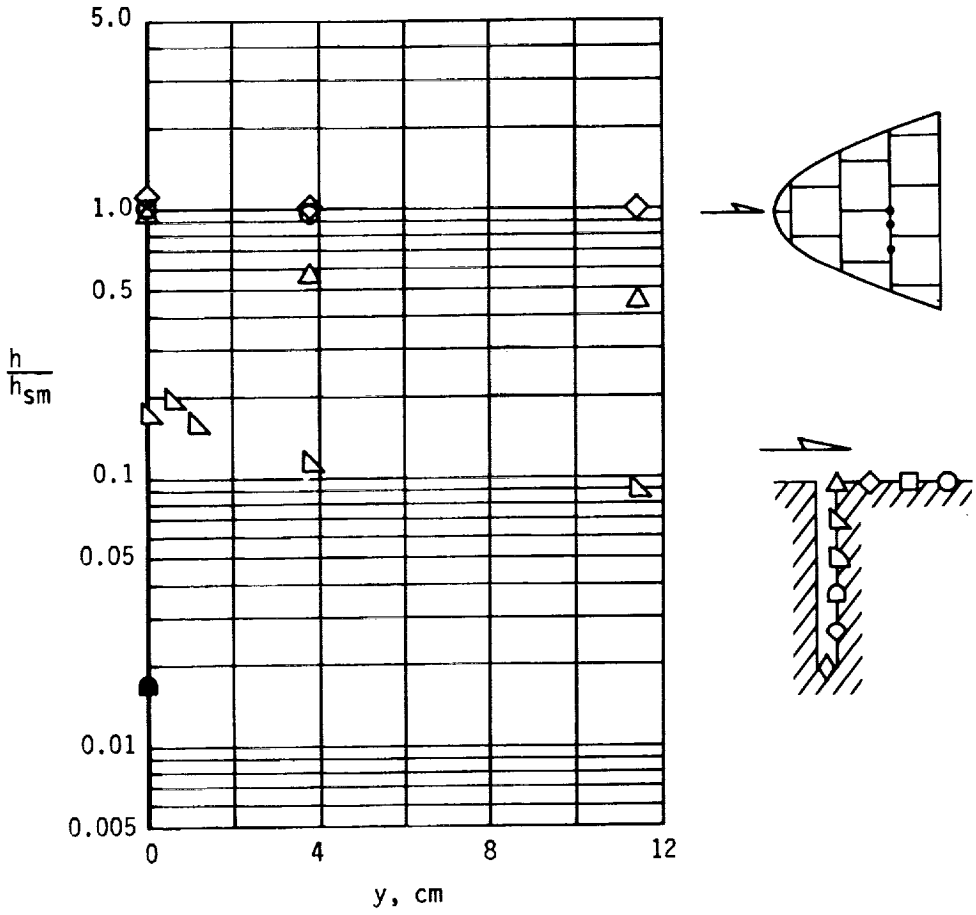

(a) $R_\infty = 1.6 \times 10^6$ per meter.

Figure 22.- Distribution of heat transfer within the transverse gap. $\alpha = 0^o$.

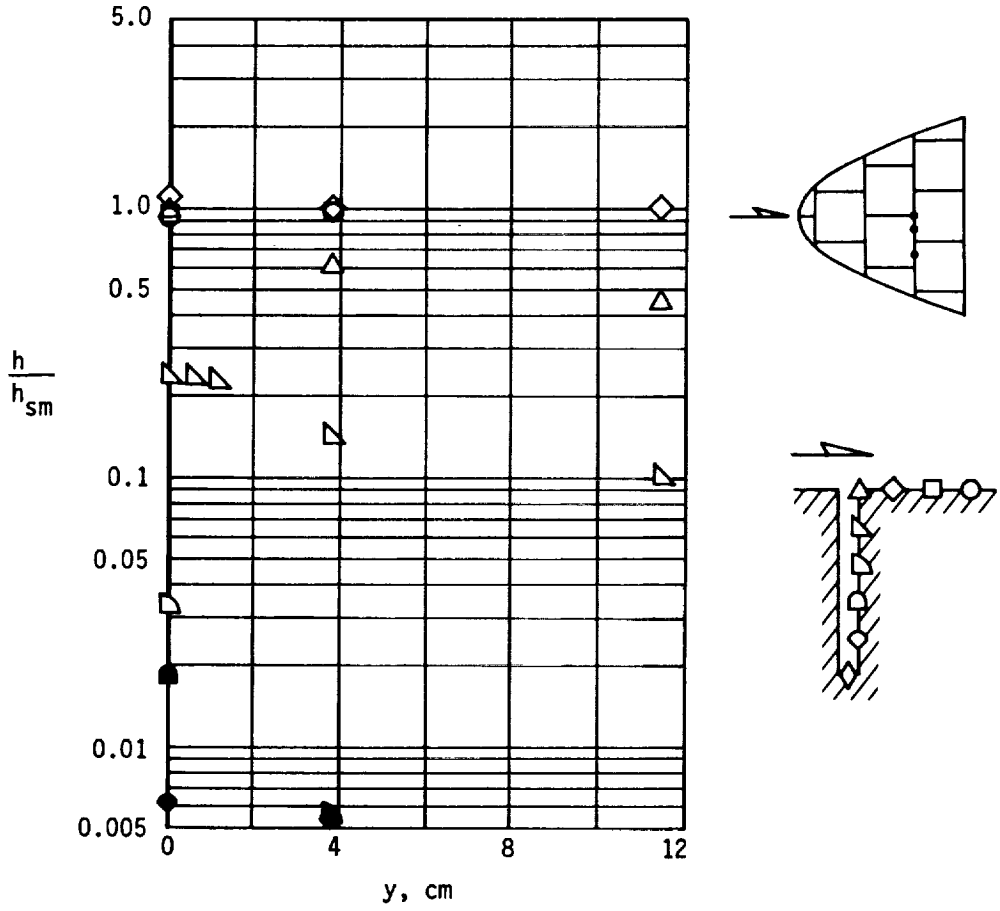

(b) $R_\infty = 3.3 \times 10^6$ per meter.

Figure 22.- Continued.

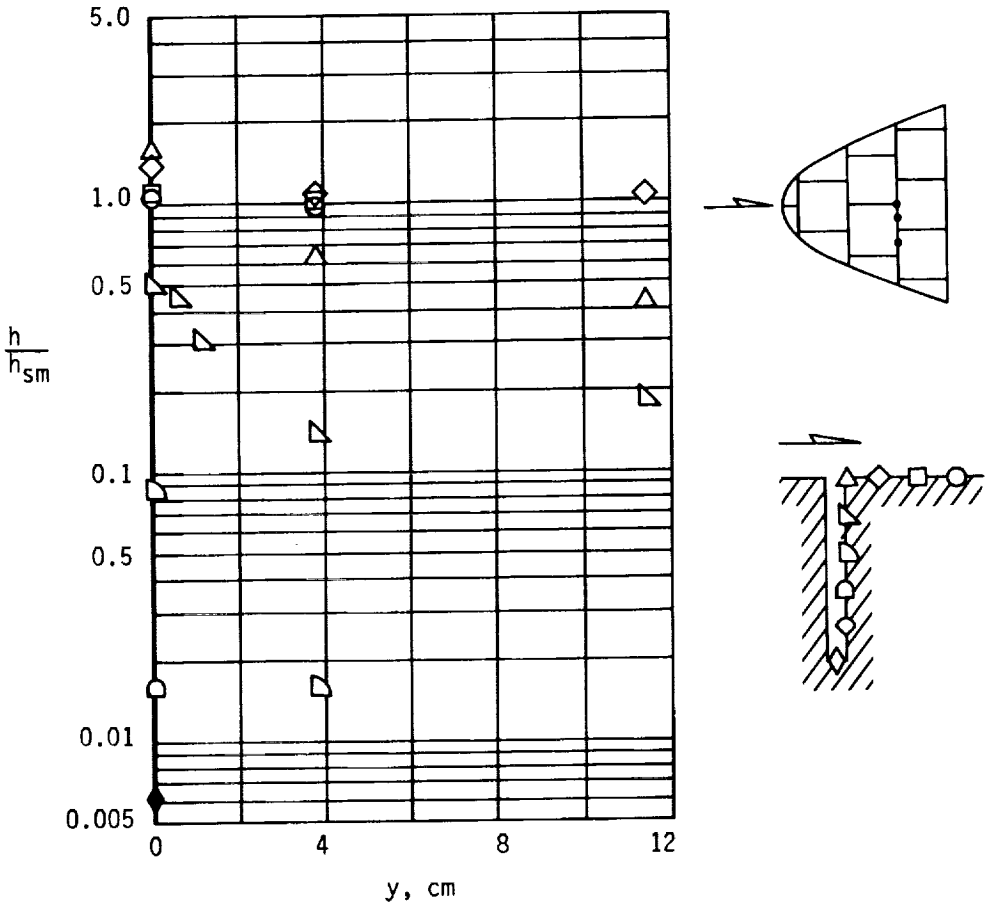

(c) $R_\infty = 6.1 \times 10^6$ per meter.

Figure 22.- Concluded.

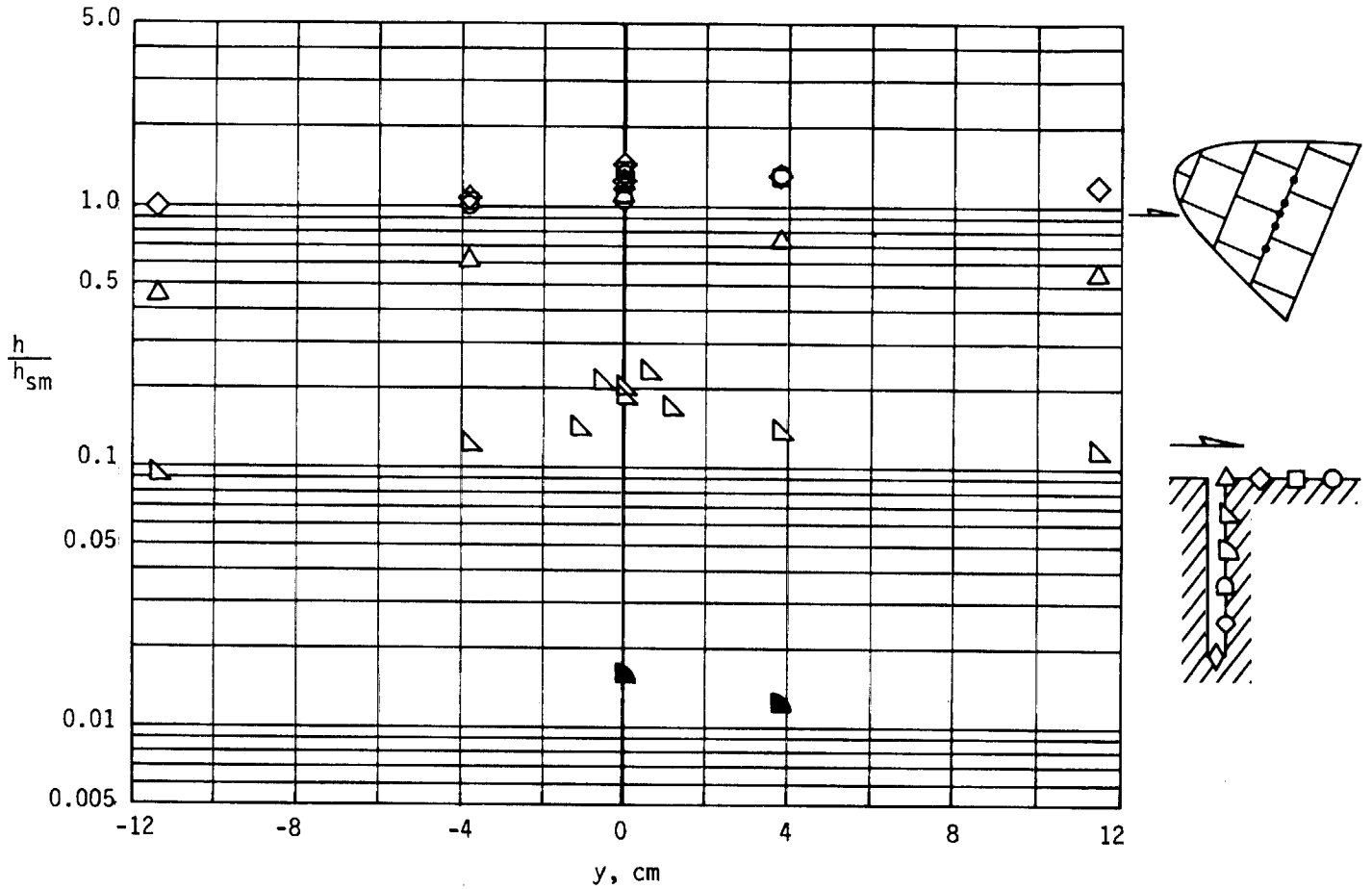

(a) $R_\infty = 1.6 \times 10^6$ per meter.

Figure 23.- Distribution of heat transfer within the transverse gap. $\alpha = 22.5^o$.

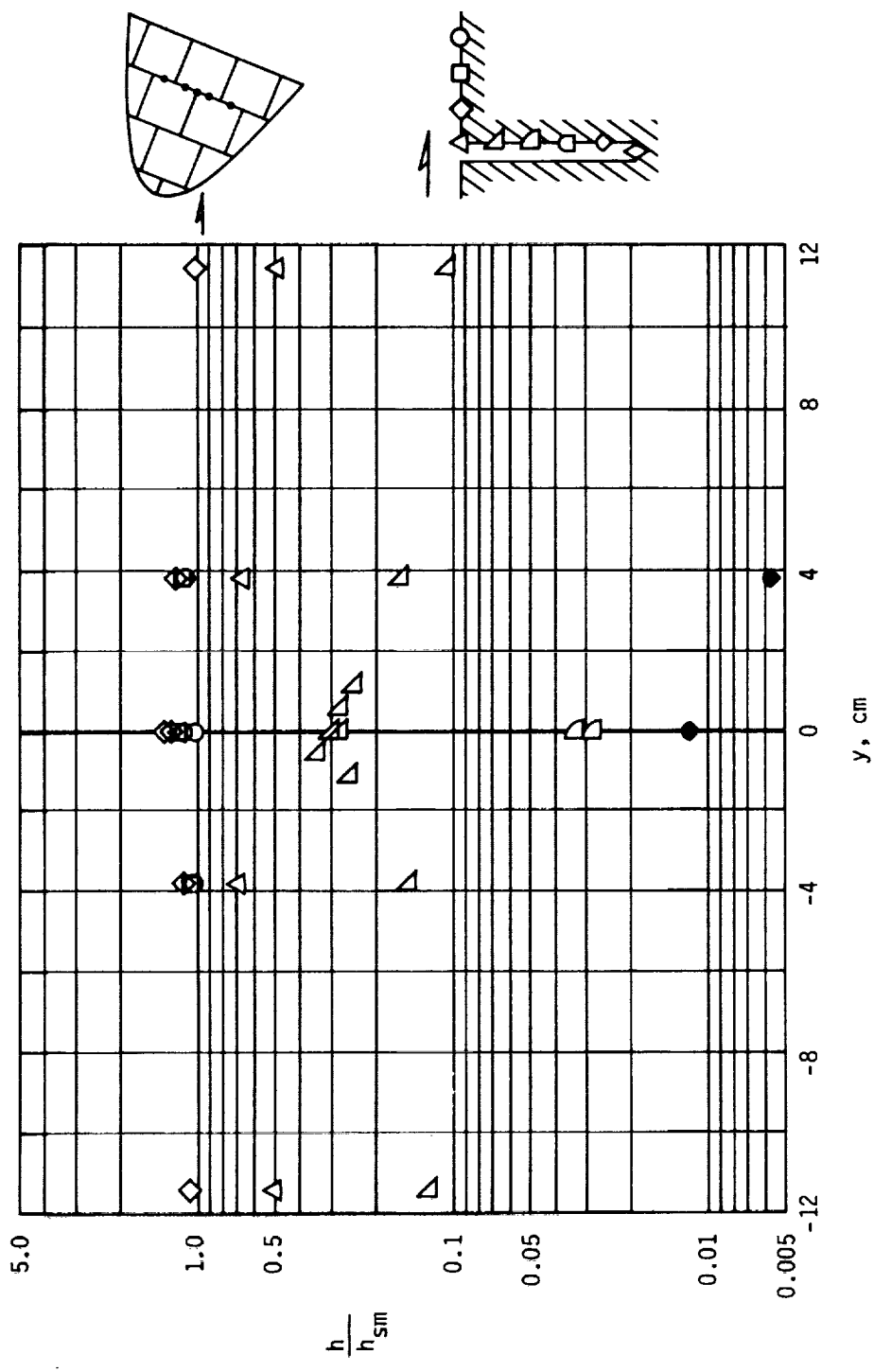

(b) $R_\infty = 3.3 \times 10^6$ per meter.

Figure 23.- Continued.

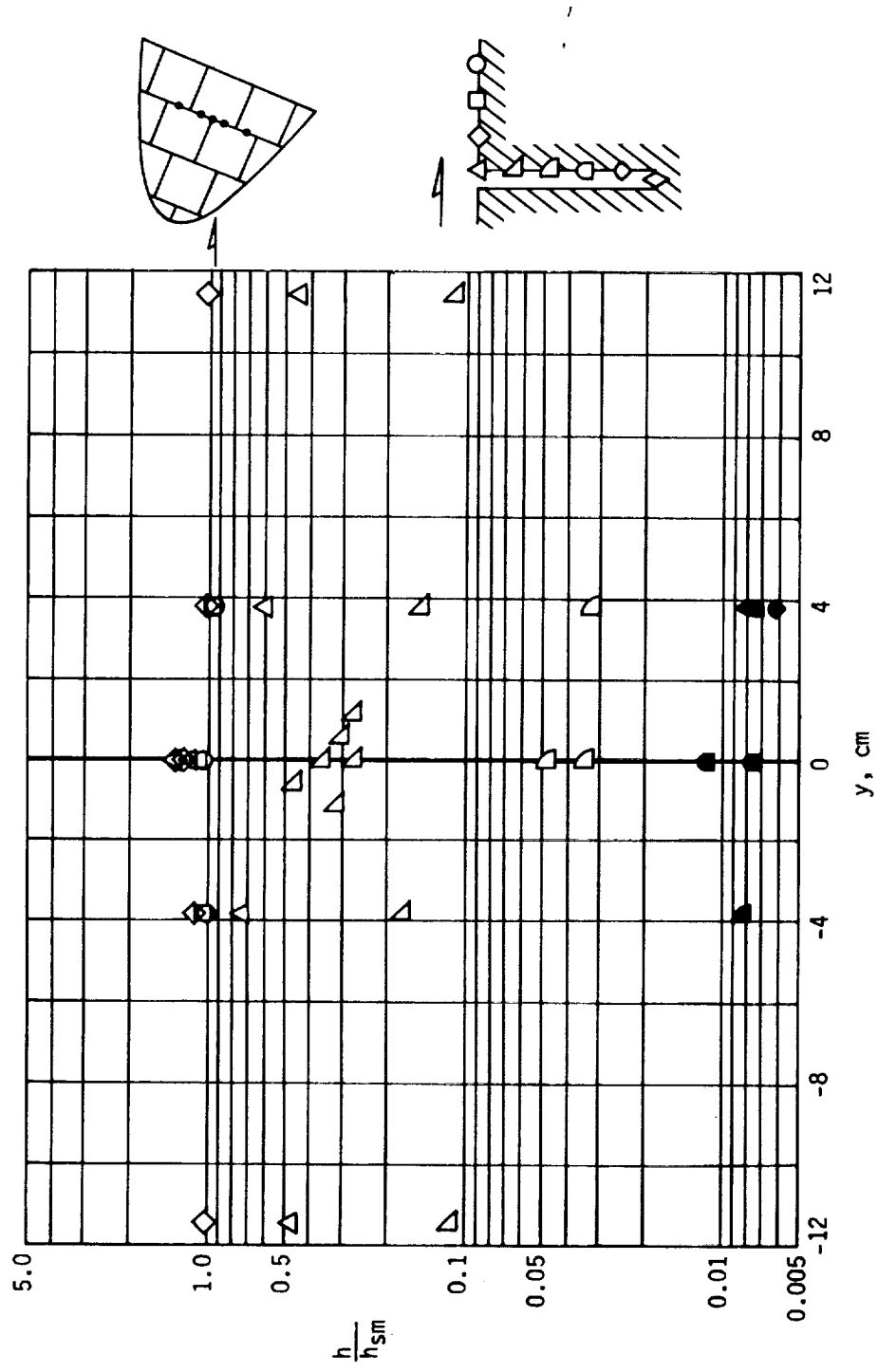

(c) $R_\infty = 6.1 \times 10^6$ per meter.

Figure 23.- Concluded.

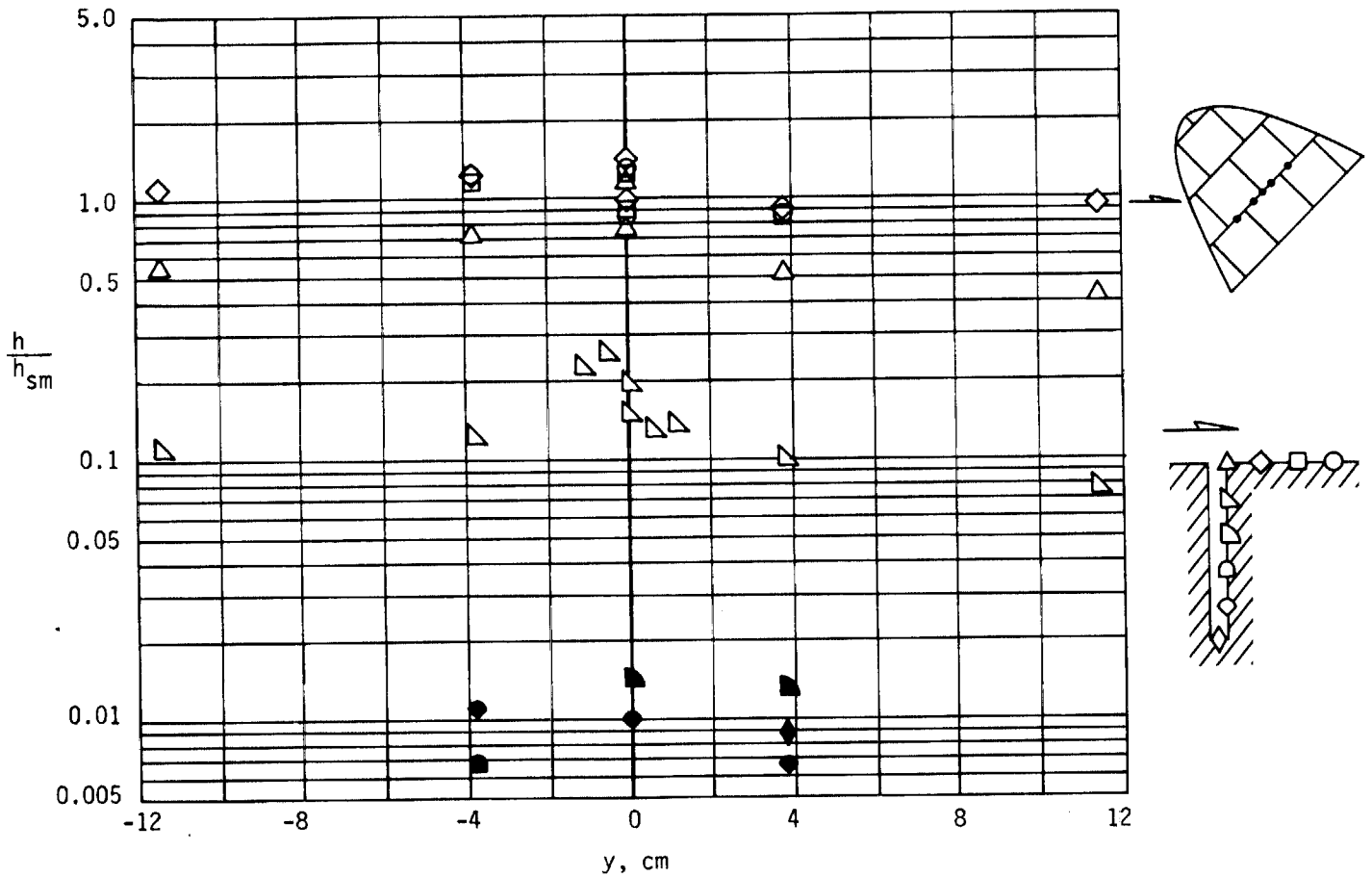

(a) $R_\infty = 1.6 \times 10^6$ per meter.

Figure 24.- Distribution of heat transfer within the transverse gap. $\alpha = 45^o$.

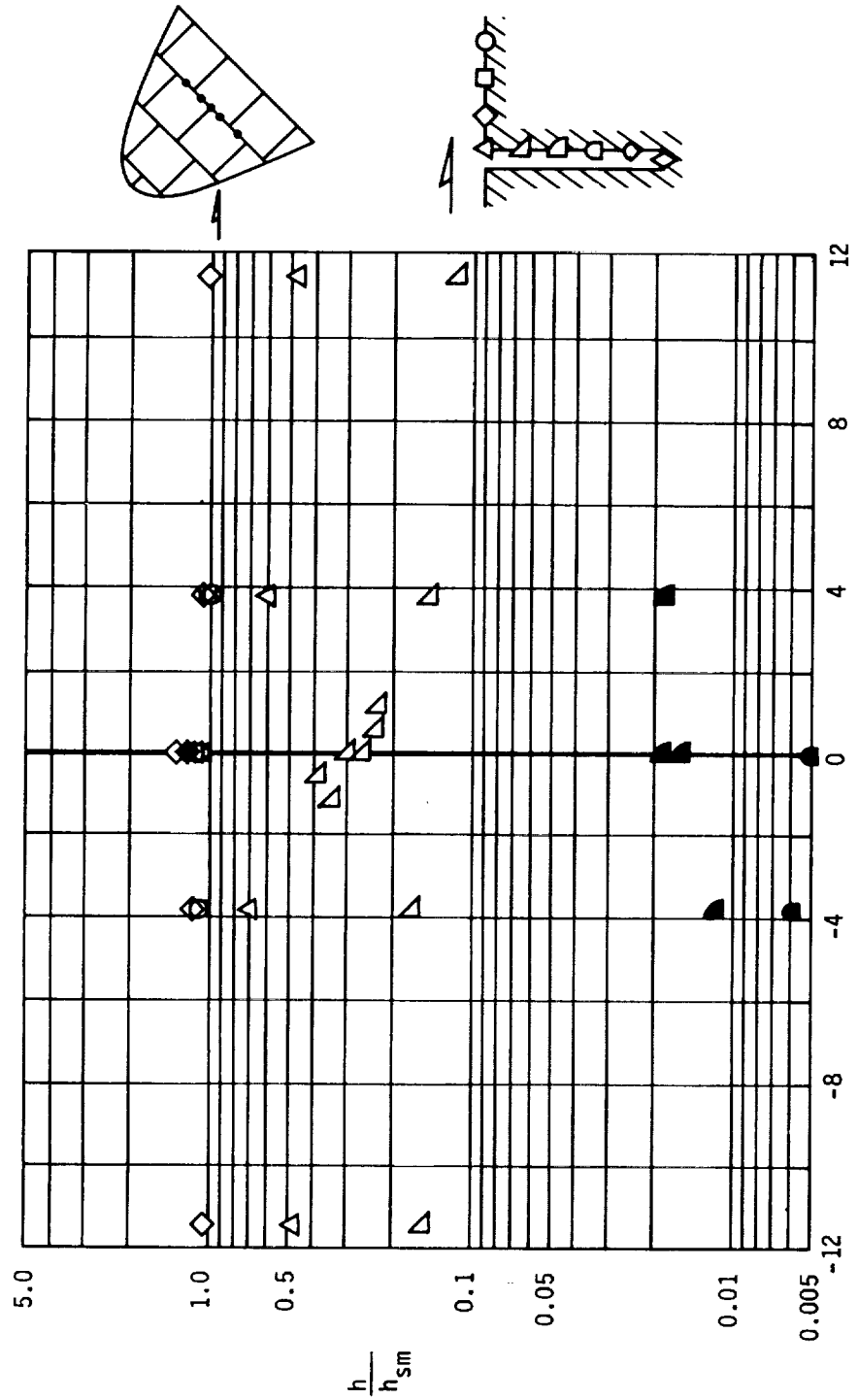

(b) $R_\infty = 3.3 \times 10^6$ per meter.

Figure 24.- Continued.

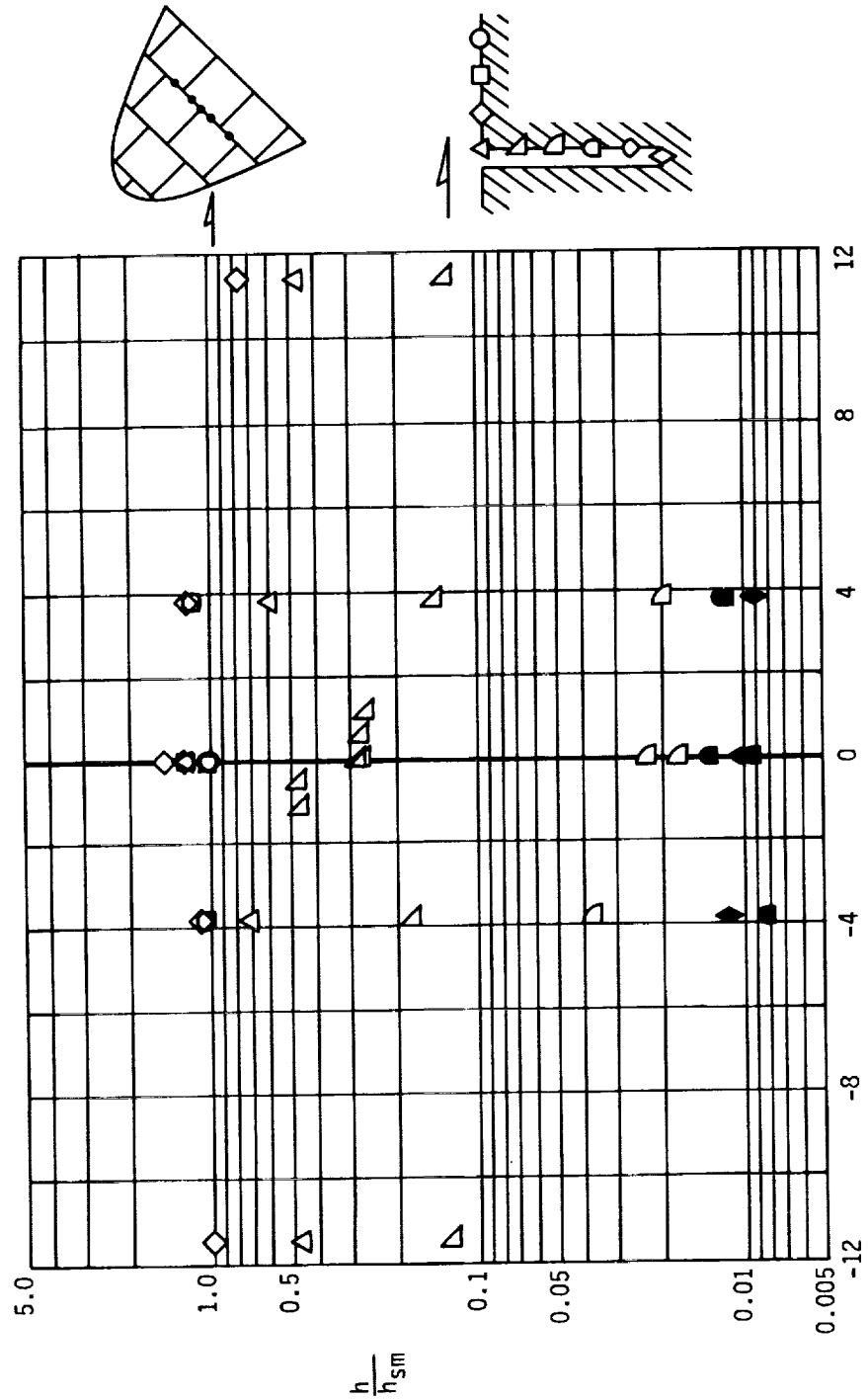

(c) $R_\infty = 6.1 \times 10^6$ per meter.

Figure 24.- Concluded.

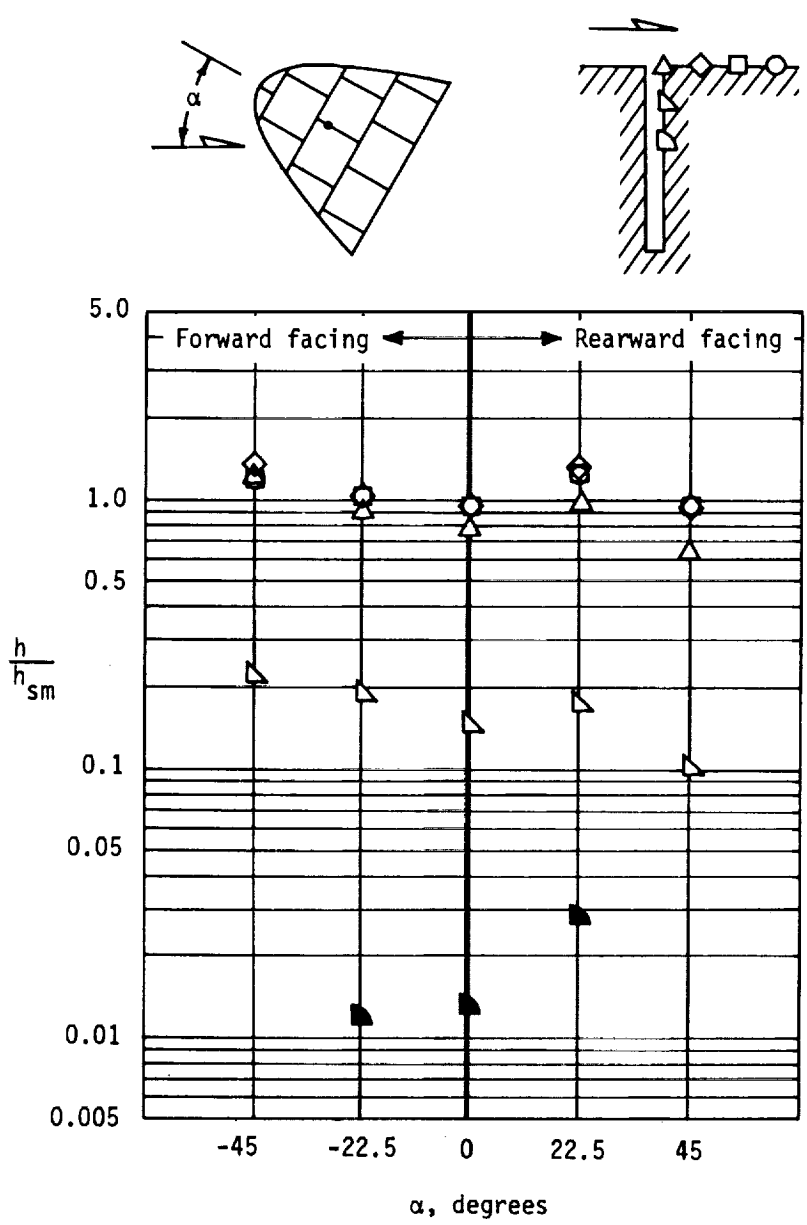

(a) $R_\infty = 1.6 \times 10^6$ per meter.

Figure 25.- Variation of heat transfer to the longitudinal gap with array rotation angle. x = -15.61 cm.

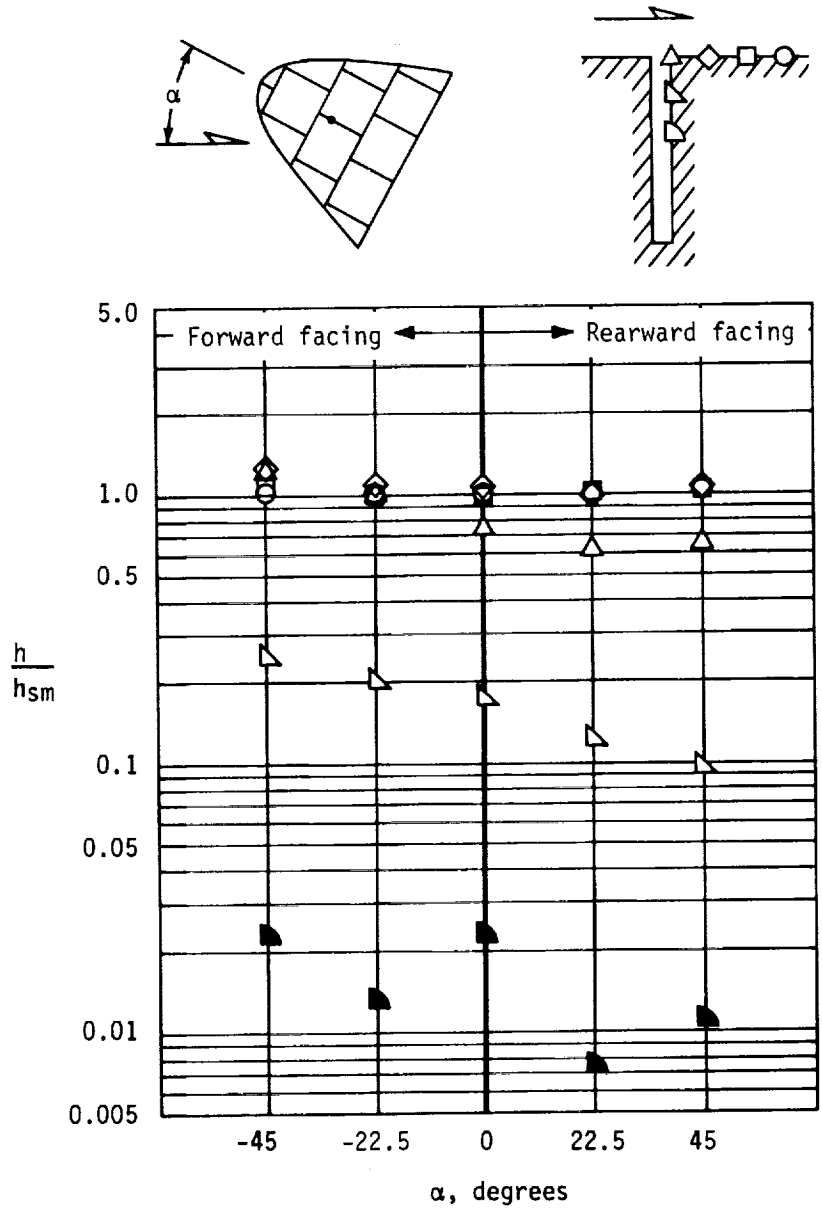

(b) $R_\infty = 3.3 \times 10^6$ per meter.

Figure 25.- Continued.

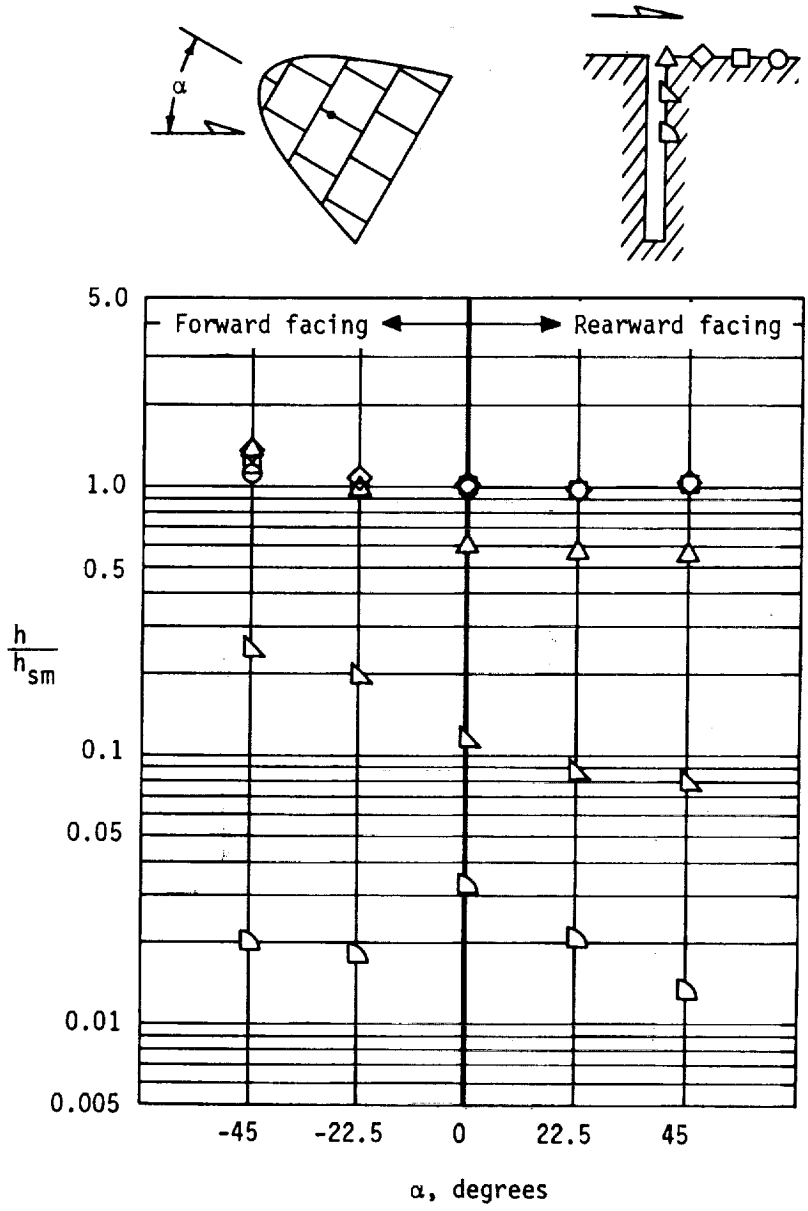

(c) $R_\infty = 6.1 \times 10^6$ per meter.

Figure 25.- Concluded.

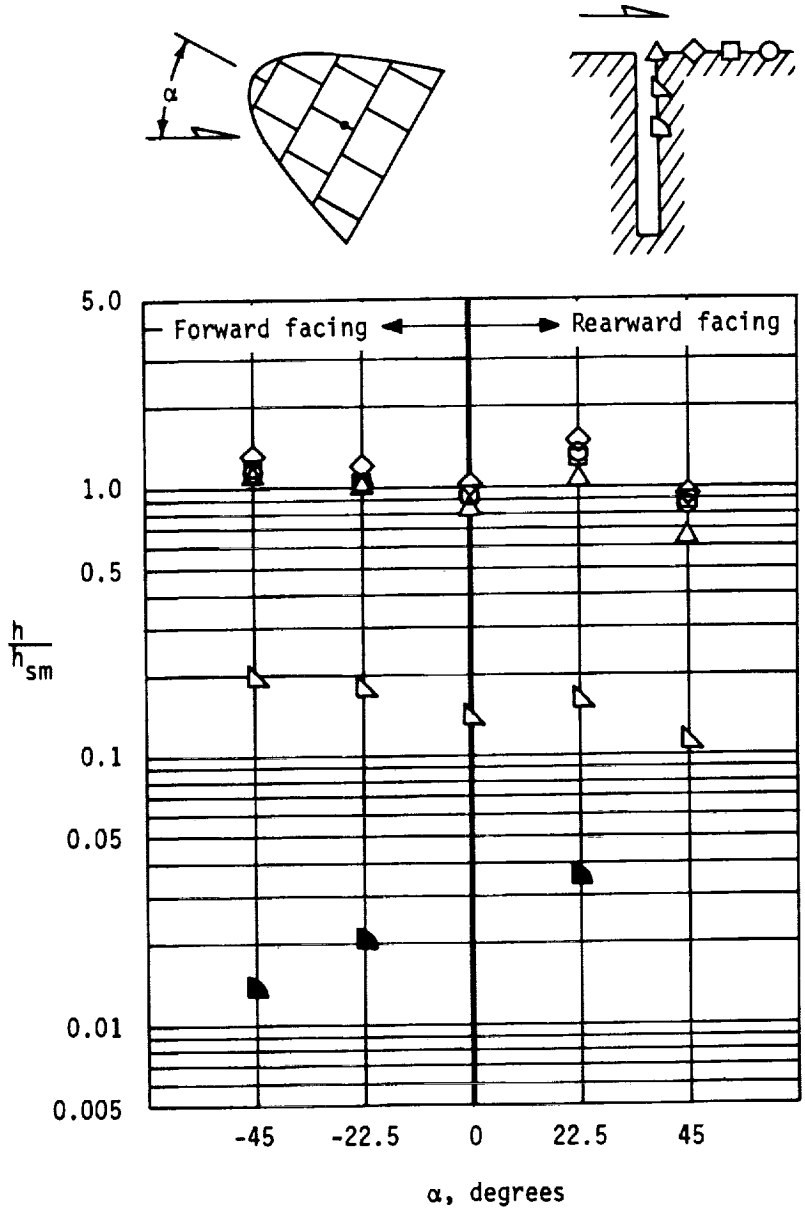

(a) $R_\infty = 1.6 \times 10^6$ per meter.

Figure 26.- Variation of heat transfer to the longitudinal gap with array rotation angle. x = 8.02 cm.

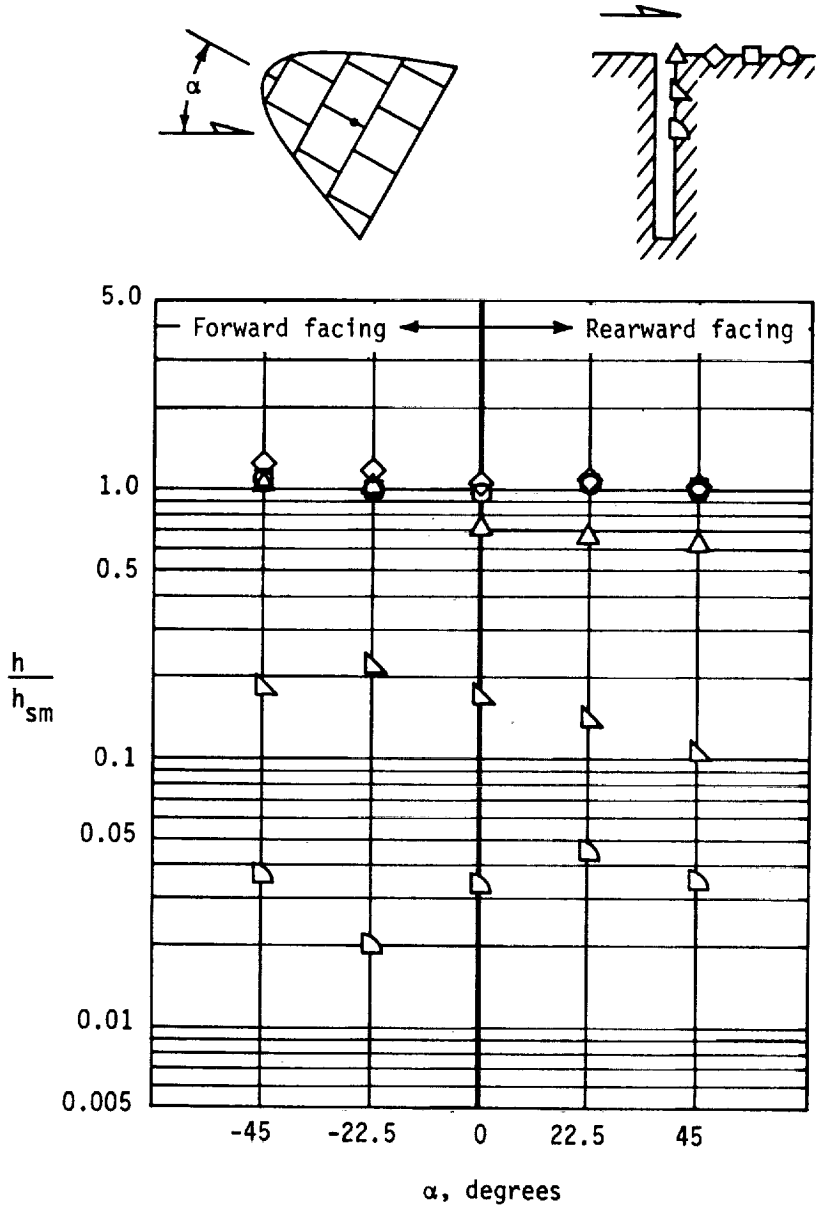

(b) $R_\infty = 3.3 \times 10^6$ per meter.

Figure 26.- Continued.

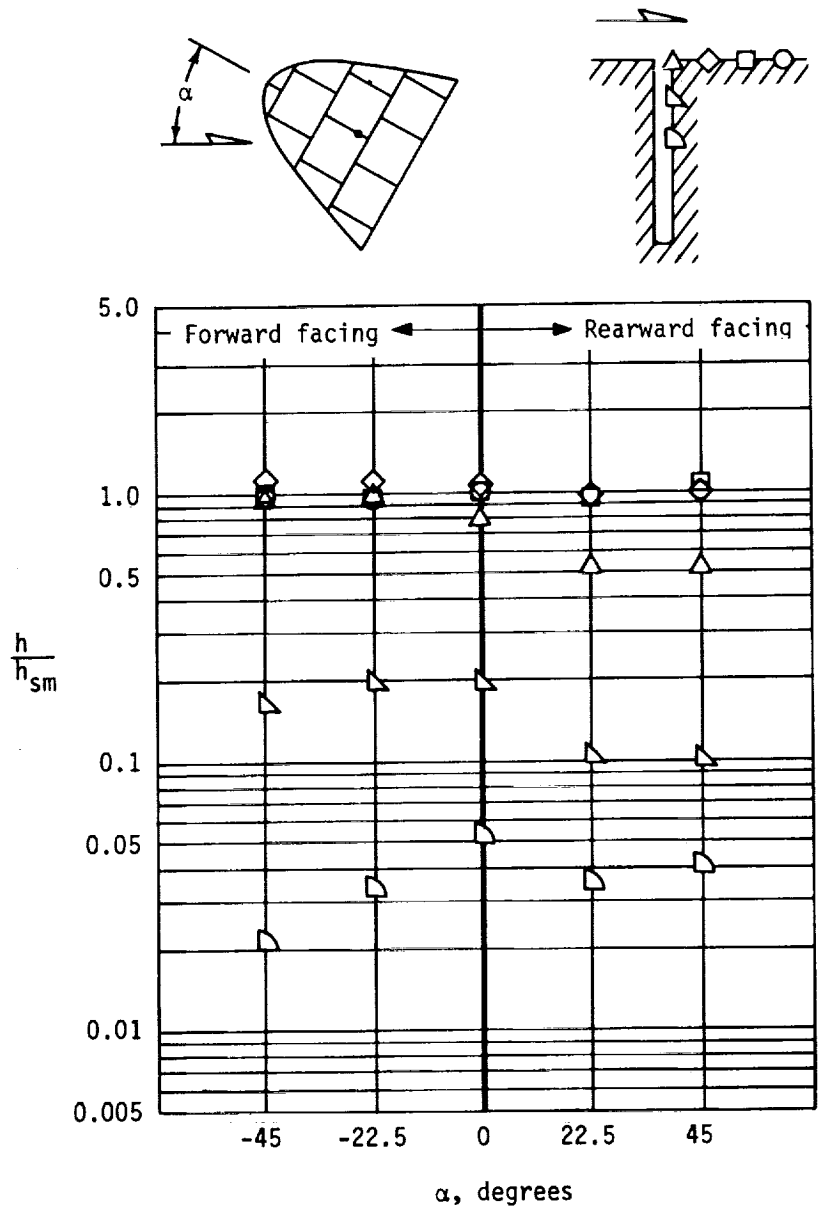

(c) $R_\infty = 6.1 \times 10^6$ per meter.

Figure 26.- Concluded.

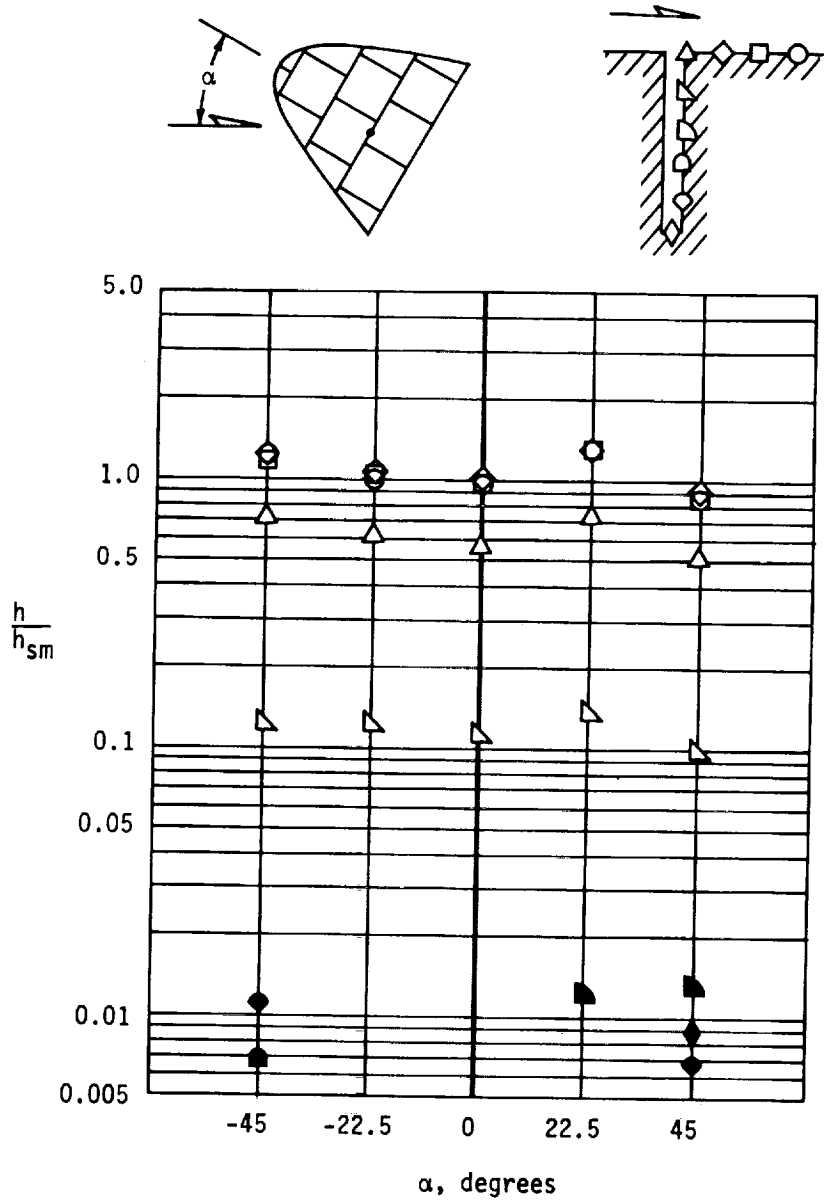

(a) $R_\infty = 1.6 \times 10^6$ per meter.

Figure 27.- Variation of heat transfer to the simple transverse gap with array rotation angle.

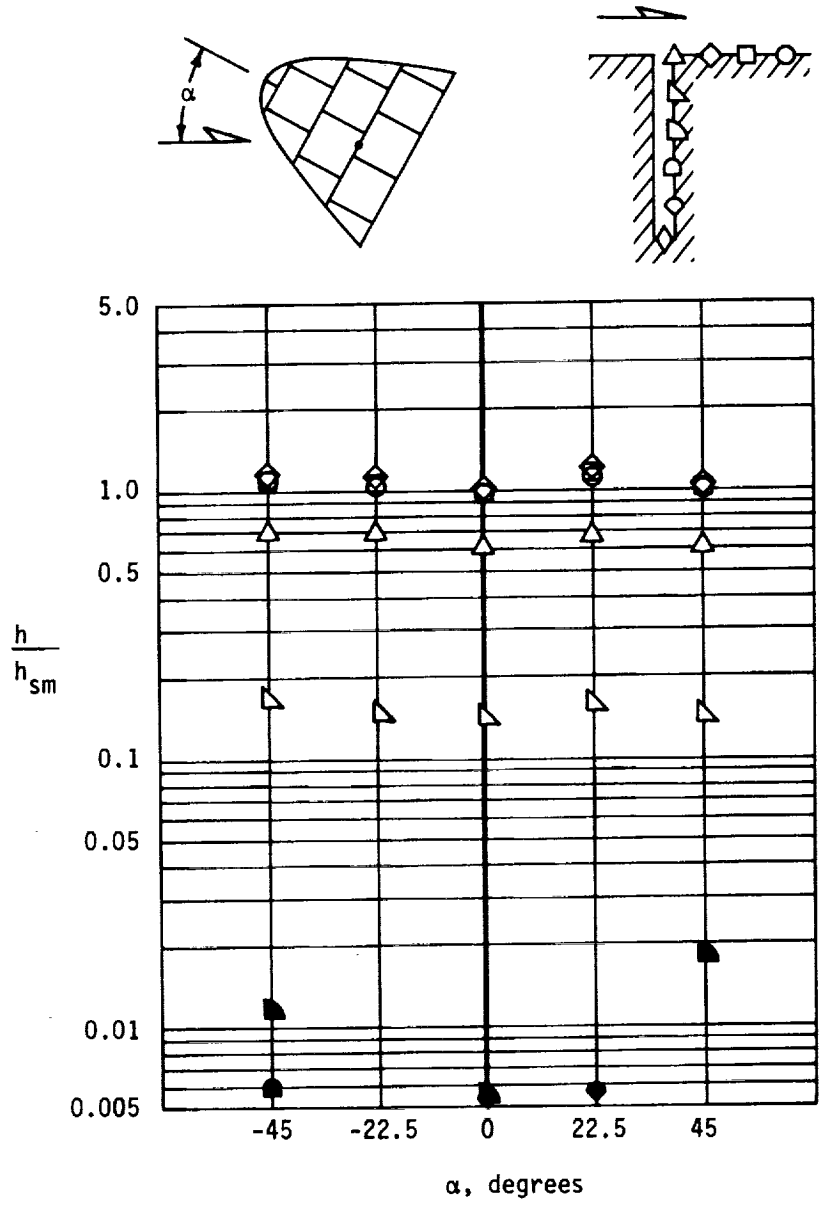

(b) $R_\infty = 3.3 \times 10^6$ per meter.

Figure 27.- Continued.

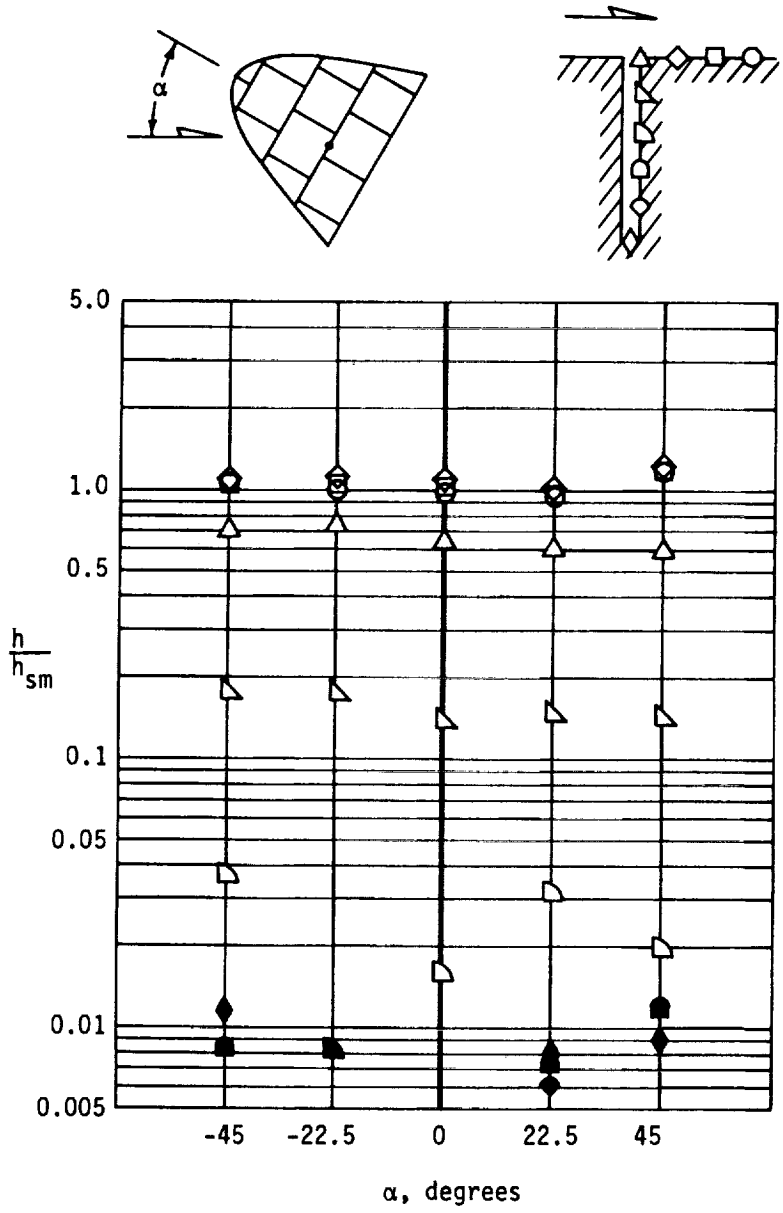

(c) $R_\infty = 6.1 \times 10^6$ per meter.

Figure 27.- Concluded.

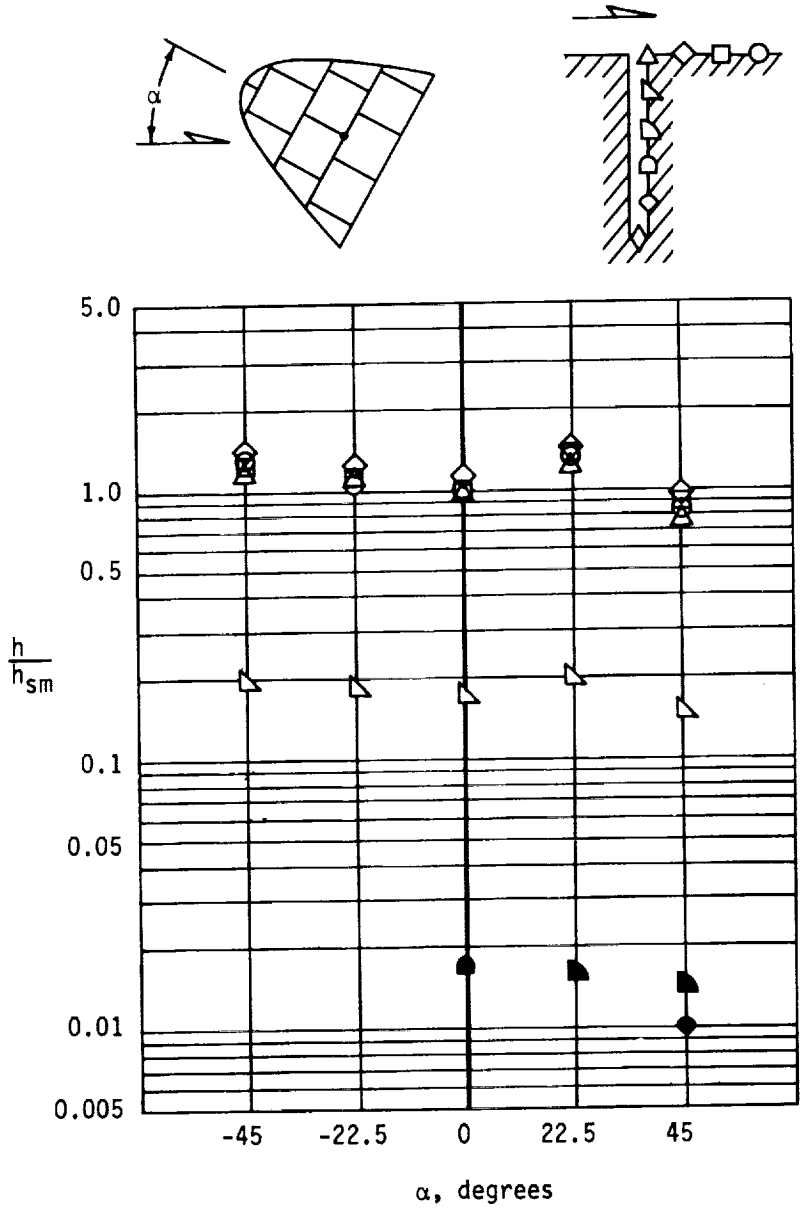

(a) $R_\infty = 1.6 \times 10^6$ per meter.

Figure 28.- Variation with array rotation angle of heat transfer to the transverse gap at its intersection with the longitudinal gap.

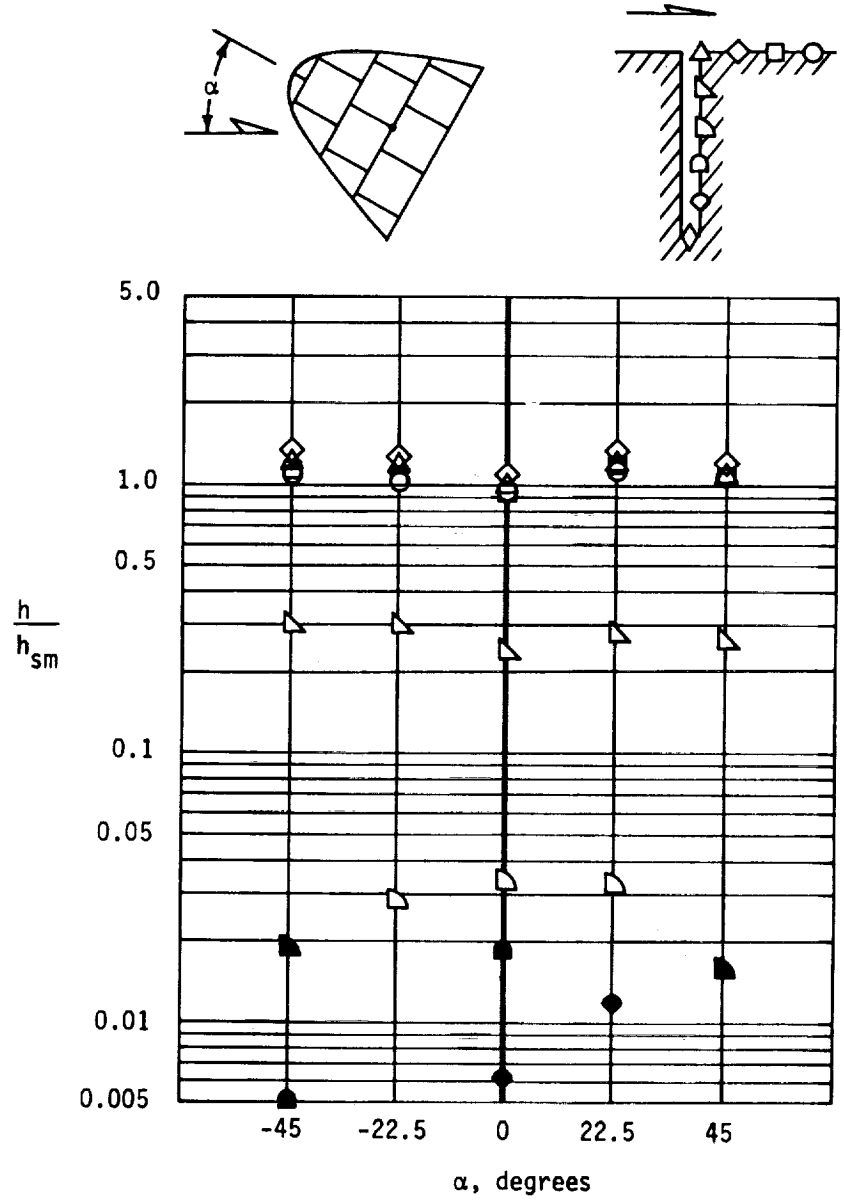

(b) $R_\infty = 3.3 \times 10^6$ per meter.

Figure 28.- Continued.

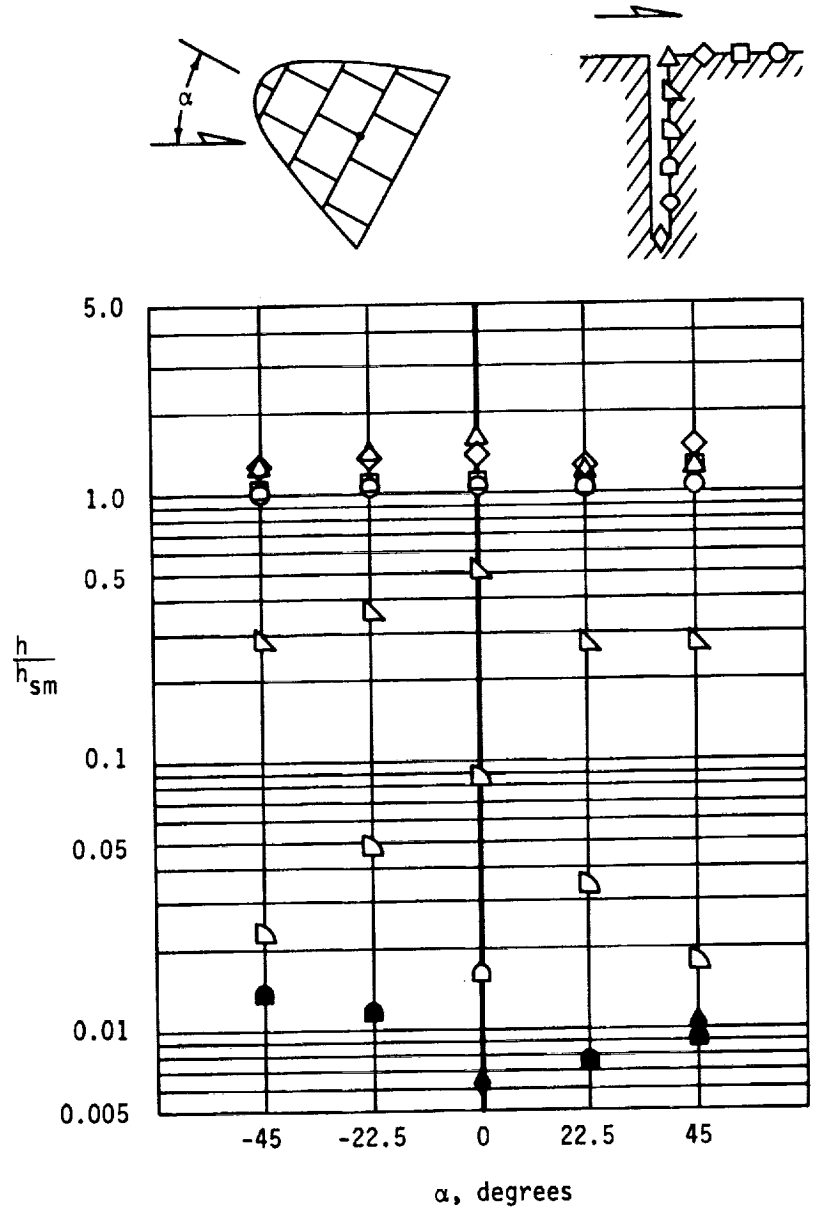

(c) $R_{\infty} = 6.1 \times 10^6$ per meter.

Figure 28.- Concluded.

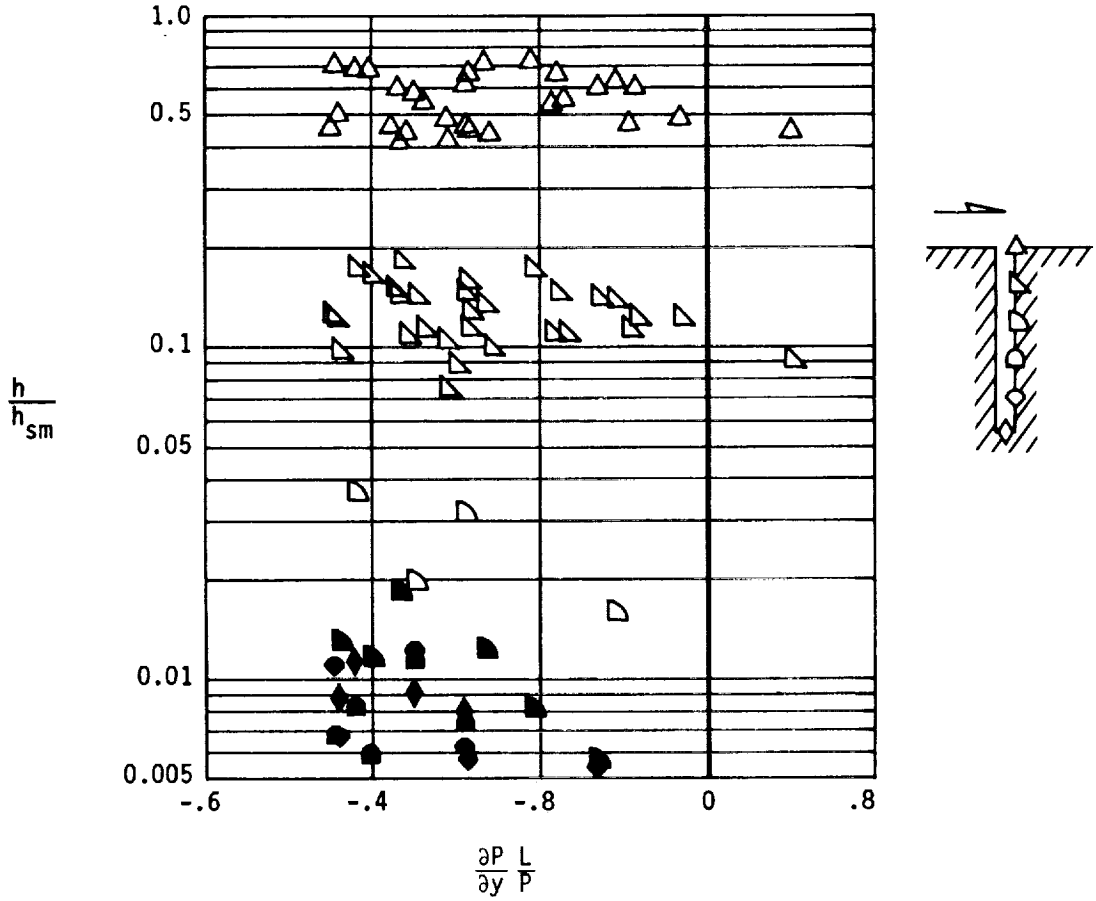

Figure 29.- Effect of pressure gradient on heat transfer to the transverse gap. y = ±3.81 and ±11.43 cm.

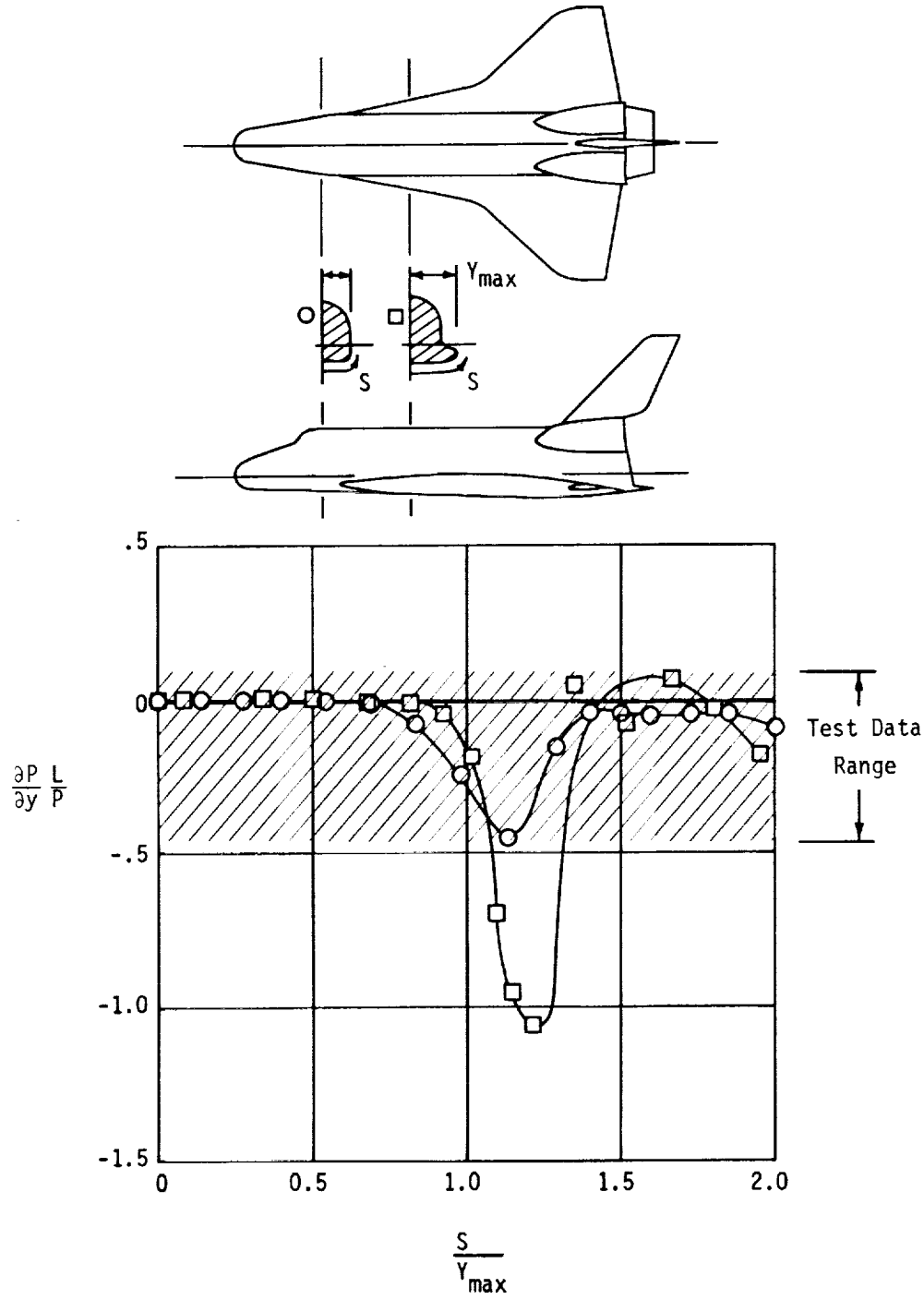

Figure 30.- Full-scale-vehicle pressure-gradient simulation. $M_\infty = 10.0$; angle of attack = 30^o.